This is the author's final accepted version.

There may be differences between this version and the published version. You are advised to consult the publisher's version if you wish to cite from it.

http://eprints.gla.ac.uk/162867/

Deposited on: 24 May 2018

Multi-Disciplinary Simulations of Stores in Weapon Bays using Scale Adaptive Simulation

G.J.M. Loupy[1] , G.N. Barakos[2]

CFD Laboratory, University of Glasgow, Glasgow, G12 8QQ, UK

N.J. Taylor[3]

MBDA UK Ltd, Filton, Bristol, BS34 7QW, UK

Abstract

This paper presents cavity flow calculations using the scale-adaptive simulation method involving door opening, store release and aeroelasticity. For established bay flows, the structural excitation showed a directional dependence, and the structures were responding to the flow frequency content. Maximum store deformations were of about 2% of the store diameter during store release. This is the first time where such effects are quantified for stores released from within bays. The store deformation, the role of the shear layer, and the store trajectory variability are also quantified.

[1]PhD Student. g.loupy.1@research.gla.ac.uk
[2]Professor, MAIAA, MRAeS, MAHS. george.barakos@glasgow.ac.uk, cor. author
[3]Capability Leader, MBDA UK Ltd., AIAA Assoc. Fellow, nigel.j.taylor@mbda.co.uk

Latin

C_x, C_y, C_z	Axial, side and normal force coefficients (-)
C_l, C_m, C_n	Rolling, pitching and yawing moment coefficients (-)
D	Cavity depth (m)
d_{mis}	Store diameter (m)
d_{ref}	Reference length (m)
f	Frequency (Hz)
f_d	Door opening frequency (Hz)
f_m^s	Modal force on solid s for the m-th mode (N/m.kg)
f_{tt}	Cavity travel time frequency (Hz)
I_x, I_y, I_z	Moment of inertia of the store $(kg.m^2)$
k	Specific turbulent kinetic energy (m^2/s^2)
L	Cavity length (m)
L_s	Store length (m)
m_s	Mass of the store (kg)
M_∞	Free-stream Mach number (-)
N_i	Number of inner timesteps (-)
n_s	Number of CFD points on solid s (-)
n_{sp}	Number of shared points (-)
n_m^s	Number of modes for solid s (-)
p, q, r	Roll, pitch and yaw rates (deg/s)
p	Pressure (Pa)
$\mathbf{p}(p, t)$	Pressure vector at a point p, and at a time t (N/m^2)
$\mathbf{P}(p)$	Position of node p (m)
$\mathbf{R}$	Rotation matrix (-)
Re_L	Reynolds number based on cavity length (-)
S	Reference area (m^2)
u, v, w	Velocity components (m/s)
t	Time (s)
$\mathbf{t}$	Translation matrix
T	Temperature (K)
U_∞	Free-stream Velocity (m/s)
W	Cavity width (m)
W_e	Maximum envelope width
$w_i(\mathbf{x})$	Interpolation weight (-)
X, Y, Z	Earth reference coordinates (m)
X_b, Y_b, Z_b	Store reference coordinates (m)
X_{dp}, Y_{dp}, Z_{dp}	Port side door reference coordinates (m)
X_{ds}, Y_{ds}, Z_{ds}	Starboard side door reference coordinates (m)
X_f, Y_f, Z_f	Fins reference coordinates (m)

Greek

α_m^s	Model amplitude of mode m of solid s (-)
Δ_μ	Statistical convergence index (-)
$\mu(t, n)$	Average of n trajectories
ω_m	Pulsation (1/s)
ϕ, θ, ψ	Roll, pitch and yaw angles (deg)
ϕ_p, ϕ_s	Port side and starboard door angle (deg)
ϕ_m^s	Normalised m-th mode displacement of solid s (m/kg)
ϕ^s	Normalised displacement of solid s (m/kg)
ρ	Density (kg/m^3)
ζ_m	Damping coefficient (-)

Acronyms

ADT	Alternate Digital Tree
$AEDC$	Arnold Engineering Development Center
CFD	Computational Fluid Dynamics
CSD	Computational Solid Dynamics
CTS	Captive Trajectory System
DES	Detached Eddy Simulation
ERU	Ejector Release Unit
HMB	Helicopter Multi-Block
IDW	Inverse Distance Weighing
LE	Leading Edge
MLS	Mean Least Square
NED	North East Down
RMS	Root Mean Square
SAS	Scale Adaptive Simulation
SPL	Sound Pressure Level
SVD	Singular Value Decomposition
TE	Trailing Edge
$6DoF$	Six-Degree of Freedom

1 Introduction

Weapon bays are used to enhance the stealth of modern military aircraft. Nevertheless, during store delivery, exposed bays generate a strong acoustic field produced by a complex interaction between the shear layer and reflected acoustic waves travelling in the bay [1, 2]. During carriage and release, stores are subjected to this unsteady flow and may undergo elastic deformations. The aeroelasticity of stores inside cavities received substantial attention in the last five years both using CFD and experiments.

Flight tests were conducted by Probst *et al.*[3] using an SUU-41 POD mounted on a F-16. A store model, with canards and fins was placed at different carriage positions inside the cavity. The store loads and accelerations were noticeably influenced by the tonal bay flow fluctuations. Wagner *et al.*[4, 5] obtained similar results in a wind tunnel, where the store was represented by a cylinder held on two support rods [4], and had a tunable natural frequency [5]. The results showed an excitation of the store at its natural structural frequencies, and at cavity modes. Near mode matching, the store response varied with changes of the store vibration by a factor two for a variation of cavity tone frequencies by about 1%. Switching to a complex cavity geometry increased the span-wise vibrations due to further asymmetries in the cavity flow [6]. Nevertheless, experiments were limited to low Reynolds numbers compared to in flight conditions, and the scaled structures were not representative of actual full scale stores.

This is where the versatility of Computational Fluid Dynamics (CFD) can aid the analysis of stores in full size weapon bays by delivering aeroelastic simulation results. Caution is, nevertheless, needed as the coupling between CFD with Computational Structural Dynamics (CSD) is loose [7], if the

deformations of the surfaces are small enough, but results may be inaccurate. For better accuracy, a strong coupling method employed by Babu *et al.*[8] transfers the loads from the CFD to the CSD grids, and sends back the deflections to the CFD grid taking into account the flow and structure history. With this method, Babu computed the fin deformations of a full size store and found fin tip displacements of 2.5 mm for the store placed near the bay shear layer. The fins were mainly excited at the structural frequencies. Table 1 summarises research works on weapon bays with store aeroelasticity.

This paper goes further, adding aeroelasticity to the store body using a full finite element model. For the first time, store releases are performed with complete store aeroelasticity, and the results are presented in five sections. First, stores were held at fixed positions at carriage and shear layer. Then, the aeroleasticity of the stores during door opening was studied. After, aeroelastic stores were released to quantify store trajectory variability with and without doors.

Study	Cavity length (m)	L/D	Store Position	Mach	Method
Arunajatesan *et al.*[7] (2013)	0.46	4.5	Carriage	0.6	Loosely coupled CSD
Wagner *et al.*[4] (2015)	0.13	3.3	Shear layer	0.59, 2.47	Exp., ideal cavity
Babu *et al.*[8] (2016)	3.33	7.0	Carriage, Shear layer, Outside	0.85	DES S-A - Strongly coupled CSD
Wagner *et al.*[5] (2016)	0.21	7.0	Shear layer	0.58, 1.47	Exp., ideal cavity
Casper *et al.*[6] (2017)	0.21	7.0	Shear layer	0.58, 0.87	Exp., ideal and complex cavities
Probst *et al.*[3] (2017)	1.02	4.0	Carriage	0.50, 0.93	Flight test

Table 1: Summary of works about aeroelasticity of store in cavity.

2   CFD method

The Helicopter Multi-Block (HMB3) [9, 10, 11] code is used in the present work. The solver is described in references [12, 13, 14, 15] and has been

extensively validated for cavity flows. DES is by far the most common way to account for the effect of turbulence in cavity flows. Nevertheless, DES is expensive, especially when several computations of store releases are required. Promising results with the SAS method [16] encouraged Babu *et al.*[12] to use this approach for weapon bay flows. Their results suggest that SAS captures the essential physics of the weapon bay, and at the same time, provides a significant reduction in CPU time by almost an order of magnitude. For this reason SAS is also used in the present work. The 6DoF method is presented in reference [17]. Only the aeroelastic method used for store deformations is shown here.

In this work, all computations were carried out using Scale-Adaptive Simulation with a timestep equal to 1% of the cavity length travel time (0.12ms). The free-stream Mach number was 0.85, and the Reynolds number based on the cavity length (Re_L) 6.5 million. The conditions approximated an aircraft flying at 3000ft, $T = 8.51°C$, $p = 89900Pa$, $\rho = 1.11kg/m^2$, and $U_\infty = 286m/s$. The computations begin with a transitional phase where the cavity flow settles. The first 10 cavity travel times of the flow, or equivalently 130ms, are ignored, and then, the flow is sampled and stored for analysis.

2.1 Geometric and Computational Model

This work considers a prismatic cavity 3.59m long, 1.03m wide, and of length to depth ratio of 7.0 (Figure 1).

The doors are modelled as solid flat plates with a thickness of 0.3% of the cavity depth, a width of 46% of the cavity width, and a length of 98% of the cavity length (Figure 1). These dimensions allow for cavity venting when doors are fully closed. ϕ_s and ϕ_p are the starboard and port side doors angles, with zero degrees corresponding to the closed doors position. CFD

(a) Bottom view - Doors closed

(b) Downstream view - Doors at 45 degrees

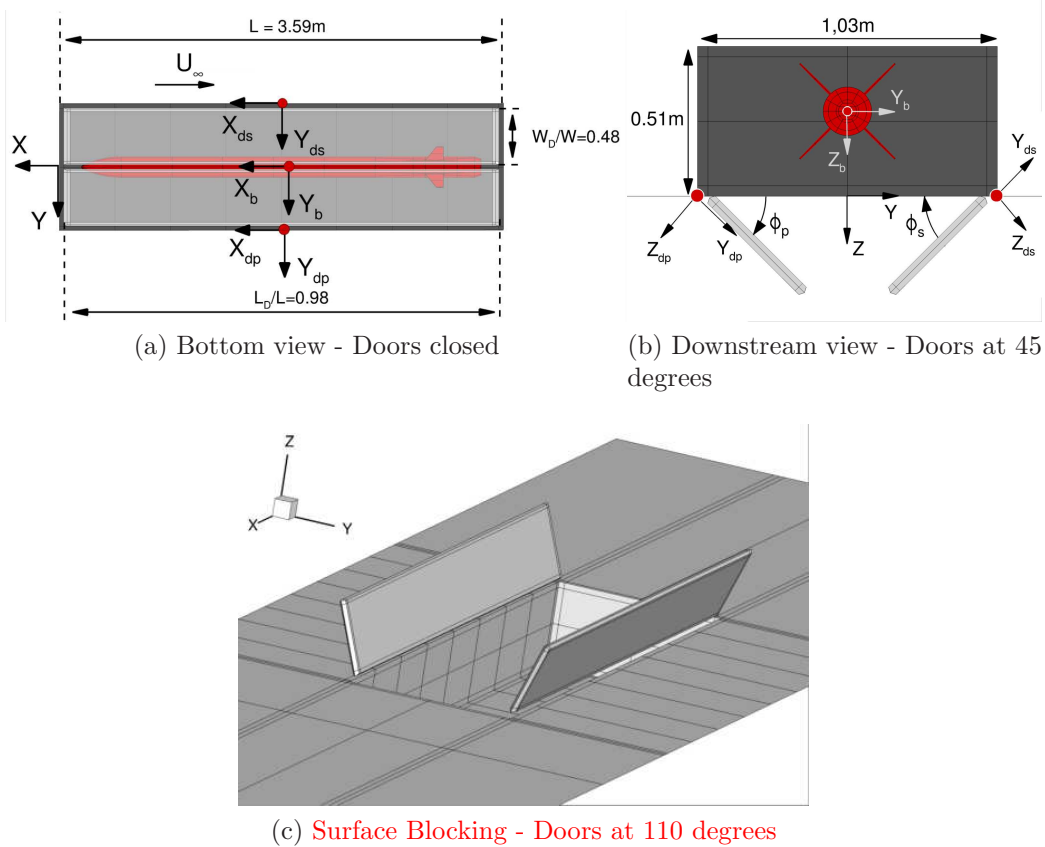(c) Surface Blocking - Doors at 110 degrees

Figure 1: Schematic of the vented cavity with store.

results at different configurations with static doors are tested and compared against computations for dynamic opening. Static door configurations include cases at 20, 45, 90 and 110 degrees. The effect of the dynamic door opening is assessed by computing the door operation for angles between 0 and 110 degrees. The doors were moving at 220 degrees/sec, and their opening was equivalent to 40 travel times at 3000 ft of altitude. The opening Strouhal number compares the door opening frequency f_d, and the travel

time frequency f_{tt} as:

$$St_{opening} = \frac{f_d}{f_{tt}} = \frac{f_d L}{U_\infty} \tag{1}$$

where L is the cavity length, and U_∞ is the free-stream velocity. Modern fighters complete the door opening during approximately 1 second, for a cavity length of about 4 meters. This corresponds using the selected CFD conditions, to a Strouhal number of 0.027, while the simulated opening speed, gives Strouhal numbers 0.047. This was selected based on earlier work [18] where fast door opening was seen to affect the store more.

The store had a mass m_s, was 90% of the cavity length, and had four fins in a cross configuration (Figure 2). The fins were supported by a rod so that they can rotate, with respect to the store body (Figure 3). The flow was resolved in the gap between the fins and the store body. The non
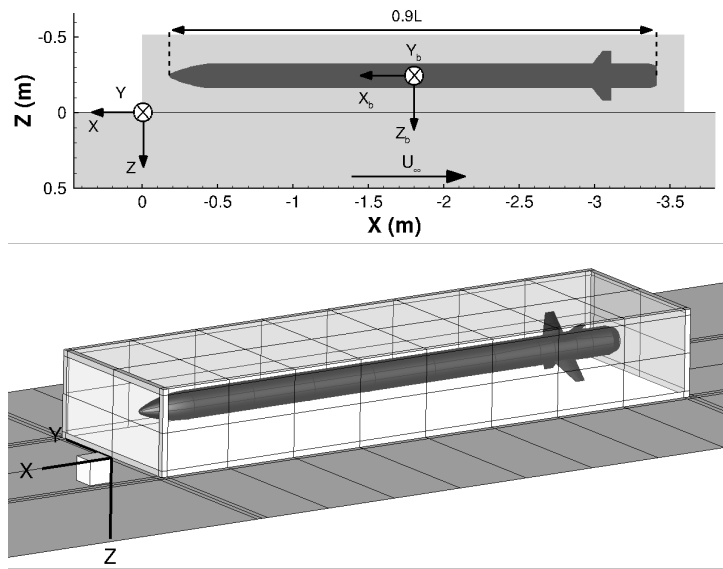

Figure 2: Geometry, cavity axes, and the store at carriage position.

(a) Perspective View

(b) Fins Position

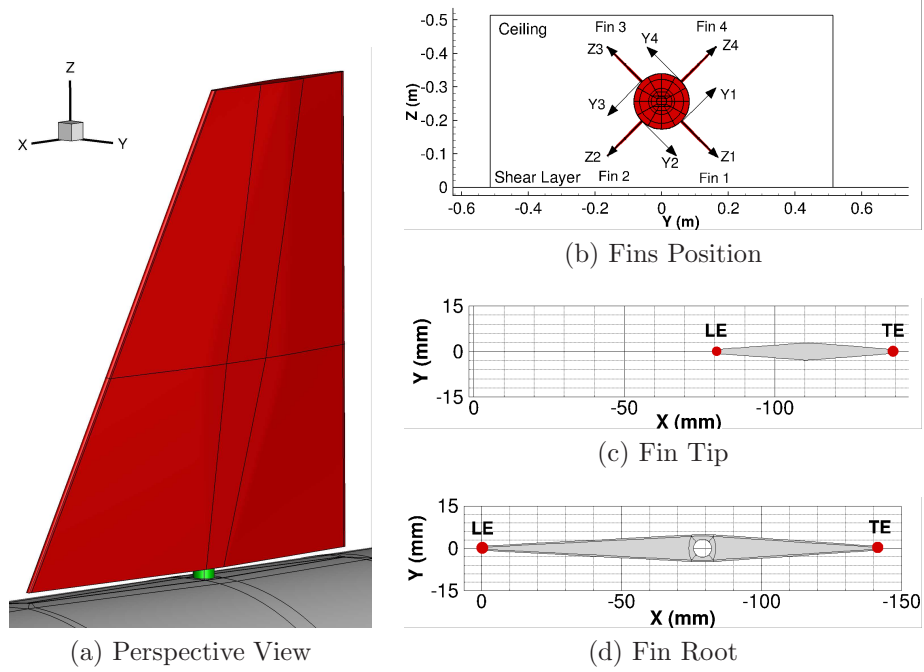
(c) Fin Tip

(d) Fin Root

Figure 3: Fin geometry.

dimensional moments of inertia $I/(m_s.L_s^2)$ were $4, 0.10^{-4}$ about the roll axis and $7, 3.10^{-2}$ about the pitch and yaw axes, with the centre of gravity located at mid length of the store. Without doors, the carriage position was at mid cavity depth (Z/D=-0.50), while the store was carried at Z/D=-0.56 allowing space for closing the doors.

All simulations were performed using the chimera technique [13] assuming one independent grid by object. Table 2 summarises the number of blocks, and the size of each grid component.

A frame of reference is attached to each solid object (cavity, door, fins, store). The cavity is attached to the earth system using the North East Down (NED) convention where, X is positive pointing north ahead of the store, Y is positive east and perpendicular to the X axis, and Z is positive towards

8

Name	Nb. of Blocks	Nb. of Points (10^6)
Cavity	1668	28.9
Door x 2	384	2.8
Store	816	7.1

Table 2: mesh size for each solid

the earth centre (Figure 1). The zero is defined at the mid-span of the front bay lip.

The store system X_b, Y_b, Z_b is right-handed and coincident with the earth system for the store at carriage, with respect to the roll, pitch and yaw axes (Figure 2). The moments are computed about the gravity center at the mid-span of the store.

The door systems X_{ds}, Y_{ds}, Z_{ds} (starboard door) and X_{dp}, Y_{dp}, Z_{dp} (port door) are right-handed and coincident with the earth system when closed, with respect to the roll, pitch and yaw axes. The moments are computed about the red dots of figure 1.

Each fin uses a local reference, where X is positive north, away of the fin, Z is positive from root to tip and perpendicular to the X axis, and Y is positive towards the port side the fin (Figure 3).

The force (C_{force}) and moment coefficients (C_{moment}) are computed using:

$$C_{force} = \frac{F}{\frac{1}{2}\rho_\infty U_\infty^2 S} \quad \text{and} \quad C_{moment} = \frac{M}{\frac{1}{2}\rho_\infty U_\infty^2 d_{ref} S} \qquad (2)$$

where F and M are forces and moments, d_{ref} is the reference length, and S is the reference area. For the store, d_{ref}, the store diameter, and $S = \pi d_{ref}^2/4$ id the store reference area. For the cavity walls and doors, $d_{ref} = L$, the cavity length, and $S = WD$ is the aft wall area.

2.2 Fluid-Structure Interaction Modelling

The aeroelastic framework of HMB3 is based on the modal method [8]. This method uses structural modes computed with NASTRAN and a mesh deformation module based on the inverse distance weighting interpolation.

2.2.1 Structural Modes

For the structural deformations, the modal approach is used to lower the computational cost. It expresses solid deformations as functions of the structure's eigenmodes. The body and fin structural modes are obtained using NASTRAN. The structural model include 23000 points on the missile and 27148 points on each fins. The structural equations are solved with the eigenvalue analysis SOL103 method of NASTRAN [19]. Four fin modes are visualised in figure 4 (modes F1 to F4 of table 3).

At carriage, the store cannot move freely. The motion of the body is constrained by the ejector release unit (ERU) holding the store at two points. The holders are modelled by two elastic elements (CBUSH) fixed to the ceiling and to the store by multiple point connections (Figure 5). The forward, and the aft hangers are respectively placed at 0.45%L and at 0.55%L from the store nose. Ten carriage modes are listed in table 3, and figure 6 shows the first six of them. At carriage, the modes and frequencies of the store are different from free flight. After the store is released from the ERU, the store can freely deform, and six other structural modes, shown figure 7, were computed.

(a) Mode F1: 144.14 Hz

(b) Mode F2: 158.05 Hz

(c) Mode F3: 232.02 Hz
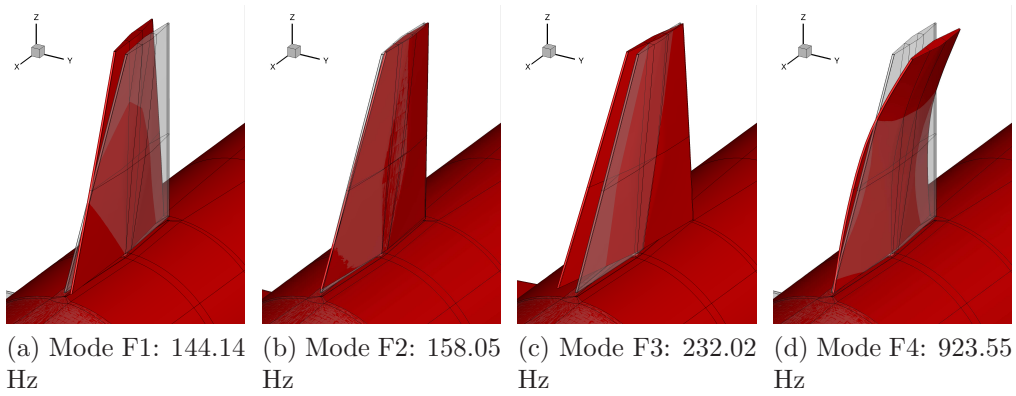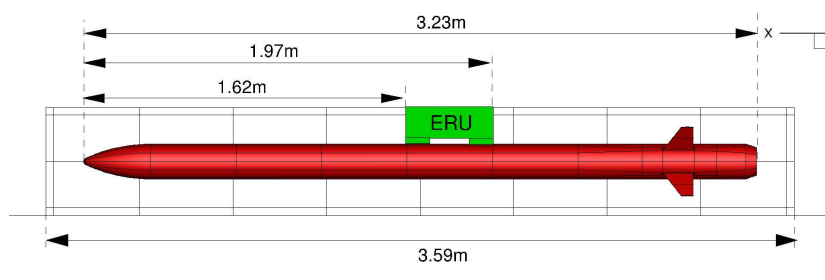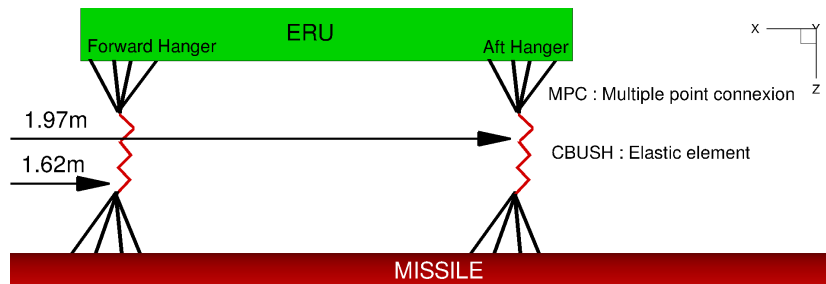
(d) Mode F4: 923.55 Hz

Figure 4: Structural modes 1 to 4 of the free root fin

(a) Position of the supports at carriage

(b) Modelling of the supports at carriage

Figure 5: Ejector Release Unit (ERU) position and structural modelling

Mode	Mode name	Frequency (Hz)	Closer Rossiter mode difference (Hz)
Free Root Fin			
1	F1	144.1	5.9
2	F2	158.1	8.0
3	F3	232.0	12.9
4	F4	923.6	15.1
Body at Carriage			
1	Y1	25.5	1.9
2	Z1	25.9	2.2
3	Y2	28.9	5.3
4	Z2	29.9	6.2
5	Y3	82.8	4.0
6	Z3	112.1	6.3
7	Y4	127.8	9.5
8	Z4	197.6	15.5
9	Y5	214.8	1.7
10	Z5	218.8	5.7
Body in Free Air			
1	FAZ1	43.4	11.7
2	FAY1	47.1	8.2
3	FAZ2	121.3	2.9
4	FAY2	148.2	1.7
5	FAZ3	259.4	14.8
6	FAZ4	440.4	6.3

Table 3: Store modal frequencies. Rossiter's modes are based on M=0.85 and L=3.59m.

(a) Mode Y1 : 25.5 Hz   (b) Mode Z1 : 25.9 Hz   (c) Mode Y2 : 28.9 Hz

(d) Mode Z2 : 29.9 Hz   (e) Mode Y3 : 82.8 Hz   (f) Mode Z3 : 112.1 Hz
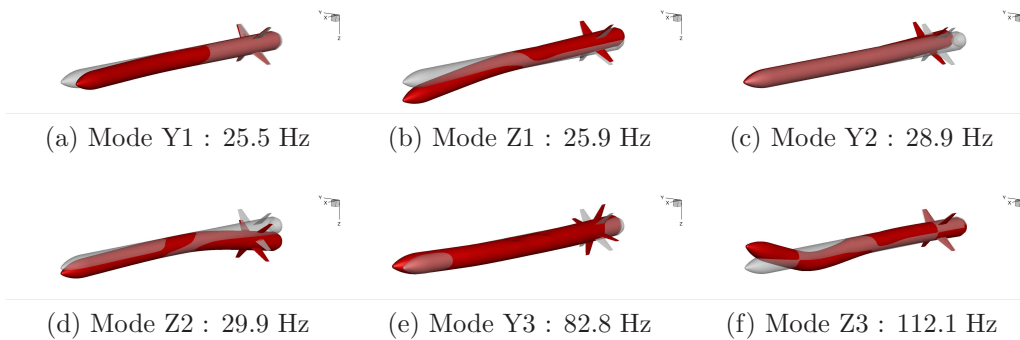
Figure 6: Structural modes 1 to 6 of the body at carriage

(a) Mode FAZ1 : 43.4 Hz   (b) Mode FAY1 : 47.1 Hz   (c) Mode FAZ2 : 121.3 Hz

(d) Mode FAY2 : 148.2 Hz   (e) Mode FAZ3 : 259.4 Hz   (f) Mode FAZ4 : 440.4 Hz
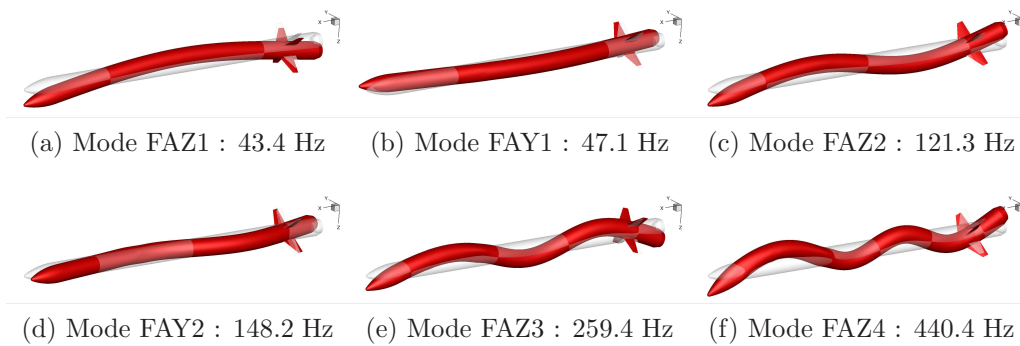
Figure 7: Structural modes 1 to 6 of the body in free air

2.2.2 CFD/CSD Interpolation

At the beginning of each computation, the structural modes are interpolated from the CSD to the CFD grid. The interpolation is performed with the Moving Least Square method (MLS). This method is accurate as loads integrations and displacement computations are carried out on the CFD grid without interpolation.

Also, the different solids in contact have to be identified relatively to each other (Figure 8) to be able to compute the motion of each fin (object 3) shown in blue, relatively to the body (object 1) shown in green. Then,

13

all shared points between fins and body are identified. Finally, a zone of size R from the shared points called patch (object 2) is defined on each fin. In the present case, R was arbitrary defined to include the complete rod in the patch.
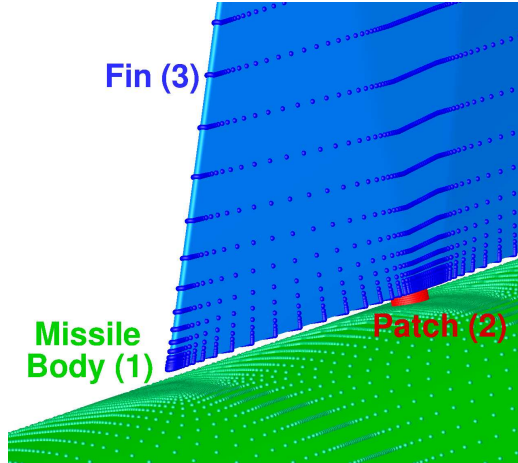

Figure 8: Body and fins structure of the store. Grid points represented by spheres.

2.2.3 Computation of the Modal Loads and Amplitudes

The CFD computation is performed on the deformed mesh to obtain the solution at $t + \Delta t$. The pressure is then summed over the undeformed mesh points to compute the modal loads $f_m^s(t)$ on the solid (s) for the m-th mode at time t:

$$f_m^s(t) = \sum_{p=1}^{n_s} \mathbf{p}(p,t).\phi_m^s(p) \tag{3}$$

with n_s the number of CFD points on the solid s, $\mathbf{p}(p,t)$ the pressure at a point p in N/m^2, and $\phi_m^s(p)$ the mode displacement at the point p for the m-th mode of the solid s normalised by the generalised mass set to 1kg. The modal load unit is $N/m.kg$.

14

The shape of the solid s, $\phi^s(t)$, is described as a sum of eigenvectors ϕ_m^s :

$$\phi^s(t) = \phi_0^s + \sum_{m=1}^{n_m^s} \alpha_m^s(t)\phi_m^s \tag{4}$$

with n_m^s the number of modes on the solid s, and ϕ_0^s the undeformed shape. The problem is then reduced to solving for the coefficient α_m^s. In the modal approach, the coefficient can be obtained by solving the following differential equation:

$$\frac{\partial^2 \alpha_m^s}{\partial t^2} + 2\zeta_m \omega_m \frac{\partial \alpha_m^s}{\partial t} + \omega_m^2 \alpha_m^s = f_m^s(t) \tag{5}$$

For stability purposes, the analysis is started with a strong damping coefficient of $\zeta_m = 0.7$ for each mode. The high starting damping in the equation is used to control the oscillations created by the step that appear at the beginning of the simulation, due to the sudden change in the forces applied to a second order system. Once the solid reaches an acceptable level of deformation, the damping is then gradually brought to a final value of $\zeta_m = 0.1$, or lower.

Then, equation 5 is explicitly solved using the leap-frog method. To ensure stability of higher modal frequencies, each timestep is solved in N_i inner timesteps of size $\Delta t_i = \Delta t / N_i$. The modal force at the time $t_i = t + i\Delta t_i$ is :

$$f_m^s(t_i) = f_m^s(t) + \frac{i(f_m^s(t + \Delta t) - f_m^s(t))}{N_i} \tag{6}$$

The m-th amplitude α_m^s is then assessed for inner timestep $t_i + 1$:

$$[\alpha_m^s]_{t_i+1} = [\alpha_m^s]_{t_i} + \left[\frac{\partial \alpha_m^s}{\partial t_i}\right]_{t_i} \Delta t_i + \frac{1}{2}\left[\frac{\partial^2 \alpha_m^s}{\partial t_i^2}\right]_{t_i} \Delta t_i^2 \tag{7}$$

15

The time derivative of the amplitudes are then computed as:

$$\left[\frac{\partial^2 \alpha_m^s}{\partial t_i^2}\right]_{t_i+1} = [f_m^s]_{t_i} - \omega_m^2 [\alpha_m^s]_{t_i} - 2\zeta\omega_m \left[\frac{\partial \alpha_m^s}{\partial t_i}\right]_{t_i} \tag{8}$$

$$\left[\frac{\partial \alpha_m^s}{\partial t_i}\right]_{t_i+1} = \left[\frac{\partial \alpha_m^s}{\partial t_i}\right]_{t_i} + \frac{1}{2}\left(\left[\frac{\partial^2 \alpha_m^s}{\partial t_i^2}\right]_{t_i} + \left[\frac{\partial^2 \alpha_m^s}{\partial t_i^2}\right]_{t_i+1}\right)\Delta t_i \tag{9}$$

2.2.4   Deformation of the Surface Mesh

The displacement of the surface of each solid is computed using equation 4. Then, the surface mesh is deformed for each solid body, beginning by the store body where the displacements are applied to all surface points. Then, the fin motion due to the body displacement is computed with the method presented in figure 9.

For each fin (f) to deform, the displacement due to the body (b) is computed as:

$$\phi^f = \mathbf{R}\mathbf{P} + \mathbf{t} \tag{10}$$

with $\mathbf{R}$ and $\mathbf{t}$, respectively, the mean rotation matrix, and the translation vector of the shared points between the fin and the body, and $\mathbf{P} = [x, y, z]$ the position of the points of fin f (Figure 9c).

The translation vector is the mean displacement of the n_{sp} shared points between the body and the fin:

$$\mathbf{t} = \frac{1}{n_{sp}}\sum_{p=1}^{n_{sp}} \phi^b(p) \tag{11}$$

with $\phi^b(p)$ the displacement of the point p imposed by the body. The centroids of the shared points are computed on the original position A, and at
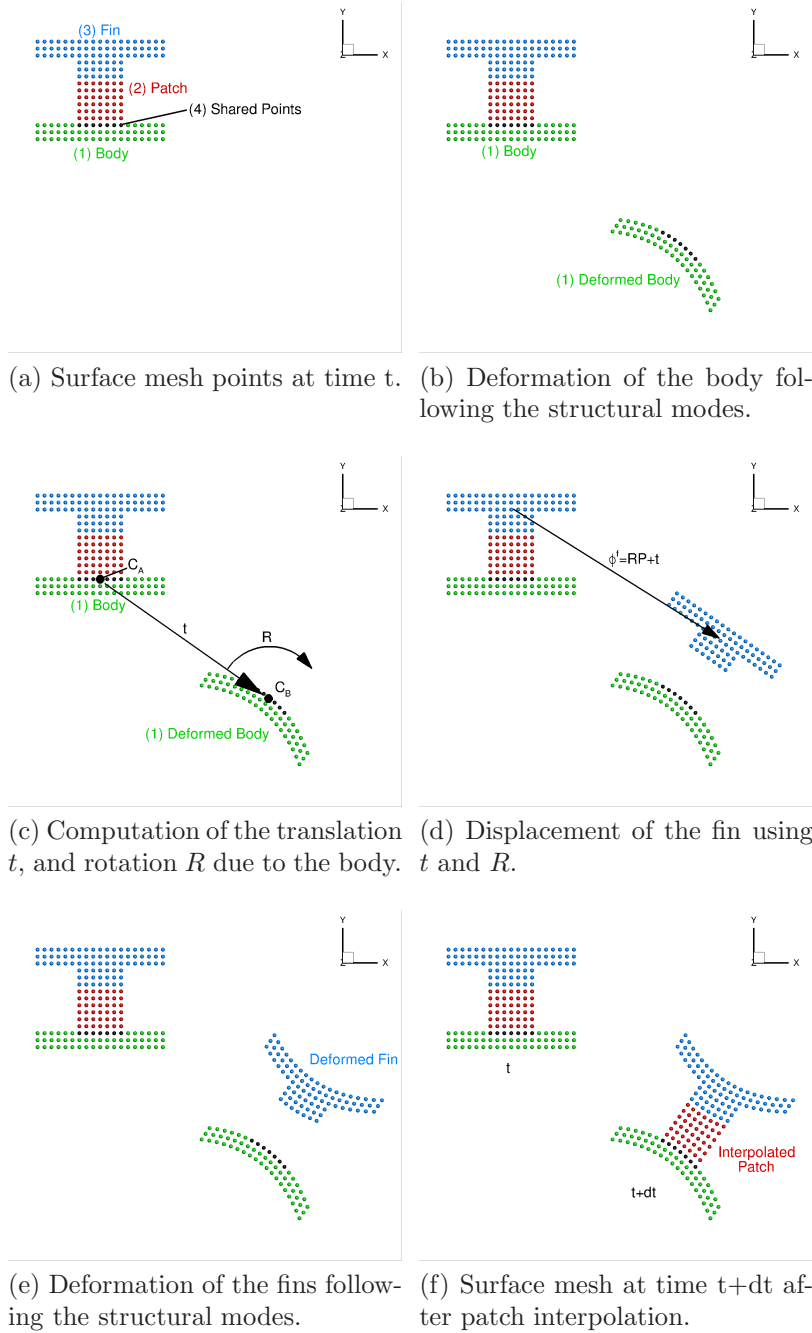
16

(a) Surface mesh points at time t.

(b) Deformation of the body following the structural modes.

(c) Computation of the translation t, and rotation R due to the body.

(d) Displacement of the fin using t and R.

(e) Deformation of the fins following the structural modes.

(f) Surface mesh at time t+dt after patch interpolation.

Figure 9: 2D example of surface mesh deformation with body and fin

17

the position B imposed by the body:

$$\mathbf{C}_A = \frac{1}{n_{sp}} \sum_{p=1}^{n_{sp}} \mathbf{P}(p) \tag{12}$$

$$\mathbf{C}_B = \frac{1}{n_{sp}} \sum_{p=1}^{n_{sp}} (\mathbf{P}(p) + \phi^b(p)) \tag{13}$$

The optimal solid rotation to go from position A to position B is computed with the Singular Value Decomposition technique (SVD). This method is fast and easy to implement [20]. The centres of rotation A and B are sent to the origin. Then, a covariance matrix $\mathbf{H}$ is computed:

$$\mathbf{H} = \sum_{p=1}^{n_{sp}} (\mathbf{P}(p) - \mathbf{C}_A)(\mathbf{P}(p) + \phi^b(p) - \mathbf{C}_B)^T \tag{14}$$

The singular value decomposition of the matrix is computed as:

$$[\mathbf{U}, \mathbf{S}, \mathbf{V}] = SVD(\mathbf{H}) \tag{15}$$

The rotation matrix is then given by:

$$\mathbf{R} = \mathbf{V}\mathbf{U}^T \tag{16}$$

Finally, the computed displacement with equation 10 (Figure 9d) and the displacement due to the structural modes are applied to the fin (f) outside the patch (Figure 9e). The displacements of the patch points are interpolated using Inverse Distance Weighting (IDW) between the fins points that just moved, and the shared points imposed by the body position (Figure 9f). This interpolation uses the same method as described in the following section

18

2.2.5.

2.2.5 Volume Mesh Deformation

To adapt the volume mesh to the surface of the deformed solid, a mesh deformation algorithm has been implemented in HMB3, based on Inverse Distance Weighting (IDW) [21]. IDW interpolates the values at given points with a weighted average of the values available at a set of known points. The weight assigned to the value at a known point is proportional to the inverse of the distance between the known and the given point. Biava *et al.*[22] used this method to optimize rotor blade shapes in HMB3, and obtained good quality mesh after mesh deformations.

Given N samples $\mathbf{u}_i = u(\mathbf{x}_i)$ for $i = 1, 2, ..., N$, the interpolated value of the function $\mathbf{u}$ at a point $\mathbf{x}$ using IDW is given by:

$$\mathbf{u}(\mathbf{x}) = \begin{cases} \dfrac{\displaystyle\sum_{i=1}^{N} w_i(\mathbf{x})\mathbf{u}_i}{\displaystyle\sum_{i=1}^{N} w_i(\mathbf{x})}, & \text{if } d(\mathbf{x}, \mathbf{x}_i) \neq 0 \text{ for all } i \\ \mathbf{u}_i, & \text{if } d(\mathbf{x}, \mathbf{x}_i) = 0 \text{ for some } i \end{cases} \tag{17}$$

where

$$w_i(\mathbf{x}) = \frac{1}{d(\mathbf{x}, \mathbf{x}_i)^p} \tag{18}$$

In the above equations, p is any positive real number (called the *power parameter*) and $d(\mathbf{x}, \mathbf{y})$ is the Euclidean distance between $\mathbf{x}$ and $\mathbf{y}$ (but any other metric operator could be considered as well).

The method in its original form becomes expensive as sample data sets get larger. An alternative formulation of the Shepard's method, which is better

suited for large-scale problems, has been proposed by Renka [23] where the interpolated value is calculated using only the k nearest neighbours within an R-sphere (k and R are given, fixed, parameters). The weights are slightly modified in this case:

$$w_i(\mathbf{x}) = \left(\frac{\max(0, R - d(\mathbf{x}, \mathbf{x}_i))}{Rd(\mathbf{x}, \mathbf{x}_i)} \right)^2, \quad i = 1, 2, ..., k. \tag{19}$$

If this interpolation formula is combined with a fast spatial search structure for finding the k nearest points, it yields an efficient interpolation method suitable for large-scale problems [21].

The modified IDW interpolation formula is used in HMB3 to implement mesh deformation in an efficient and robust way. The known displacements of points belonging to solid surfaces represent the sample data, while the displacements at all other points of the volume grid are computed using equation (17) with the weights of equation(19). For fast spatial search of the sample points, an Alternating Digital Tree (ADT) data structure [24] is used. A blending function is also applied to the interpolated displacements, so that they smoothly tend to zero as the distance from the deforming surface approaches R.

3 CFD Validation

3.1 Cavity Flow Validation

Simulations were first carried out for the M219 cavity [25]. M219 has a length to depth ratio of 5, a width to depth ratio of 1, and a length of 0.51m. Experiments were carried out by Nightingale *et al.*[25] at Mach 0.85, and a Reynolds number Re_L, based on the cavity length, of 6.5 million. The

cavity has two doors attached at its sides at an angle of 90 degrees. Data was obtained using Kulite^{TM} pressure transducers at the cavity ceiling. CFD results for three grid densities of 13, 22 and 34 million points are compared to the experimental data for the cavity with doors. The computations used a dimensionless time-step of 0.01, and the SAS model [26].

Three tests at the same conditions, named S1, S2 and S3 were performed for the M219 cavity with doors. They were sampled at different frequencies and have different durations. Table 4 presents a summary.

Name	Signal length (Travel Time)	Sampling (kHz)	Date
No Doors	1910	6.00	Oct 1991
Doors S1	1831	31.25	Sep 1999
Doors S2	16798	6.00	Mar 2001
Doors S3	1910	6.00	Sep 1999

Table 4: Available signals for CFD comparison.

Figure 10 shows the SPL and OASPL at the ceiling mid-span for the different experimental data sets computed using the raw data. Vertical lines represent the Rossiter modes[27]. The SPL shows strong tones close to Rossiter modes 1, 2, 3 and 4 and a strong broadband noise. There is a finite number of tones of different amplitudes, and their distribution is not harmonic. S1 and S2 have similar SPL, and show less than 2dB differences in the OASPL. However, run S3 is different by 40dB in frequency, and 4dB in amplitude for the tones. In addition, the OASPL is 3dB lower at the cavity front. Short runs with small frequency sampling as S3 are not necessarily identical as cavity flow fluctuations are not periodic, and contain strong broadband noise. This shows that measurements of cavity flows are difficult and need long signals sampled at high rate. For CFD comparisons, run S2 is employed as it
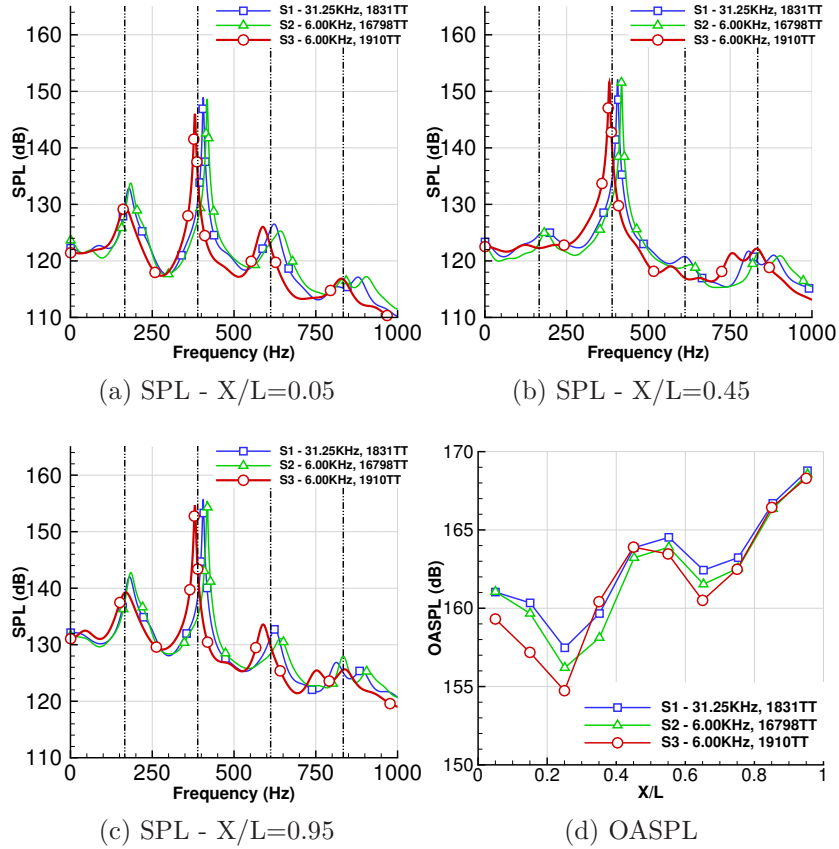
21

(a) SPL - X/L=0.05

(b) SPL - X/L=0.45

(c) SPL - X/L=0.95

(d) OASPL

Figure 10: M219 with door SPL and OASPL for three experimental signals.

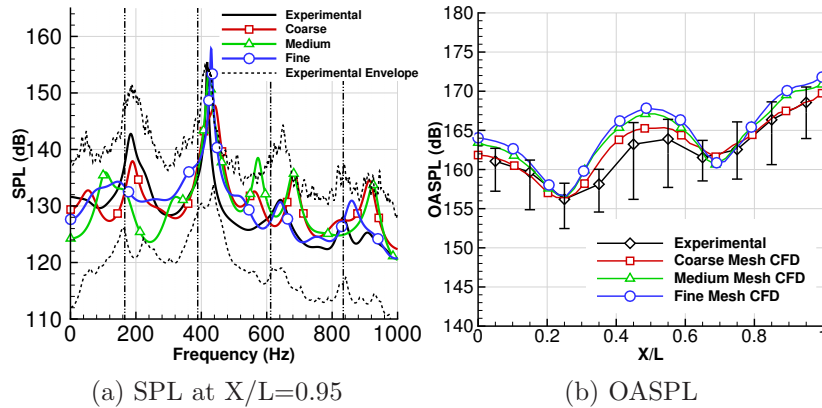(a) SPL at X/L=0.95

(b) OASPL

Figure 11: M219 with door noise at ceiling mid-span for CFD and experiments.

is the longest signal, and it agrees with the over-sampled signal S1 obtained two years earlier [25]. Past works [2, 17] were using signal S3 for comparison with CFD, and for this reason, the envelope, and peak values appear to be slightly different than what is shown in figure 11.

Since the CFD simulations are run for a typical length of 25 cavity travel times, and run S2 spans 16798 travel times, the comparison is carried out as follows. The experiment is divided in windows of 25 travel times, and the minima and maxima over all the windows are reported in figure 11 as envelope and vertical bars. This shows large fluctuations between each experimental segment with an amplitude of 30dB in SPL, and 10 dB in OASPL. Figure 11a shows the SPL comparison between CFD and experiments at 95%L on the cavity ceiling mid-span. The vertical black lines represent Rossiter's modes. The SPL results are in better agreement with the test data when the fine grid is used, capturing both tonal and broadband noise. The OASPL, on figure 11b is shown at cavity mid-span. The second Rossiter mode is dominant, with a W shape of the OASPL, as captured by the CFD and the experiments [28]. There is convergence towards the fine mesh solution, with a small relative difference of 1 dB between medium and fine grids.

There is a small overestimation of the OASPL, all along the cavity length. A large number of simulations performed with various models [29, 30, 31] had similar overestimation. This may be due to experimental errors, the signal length, limitations of the SAS [26] and DES [32] approaches, and simplifications in the CFD setup for this case.

3.2 Validation of the Six Degree of Freedom Simulation Method

This section presents additional validation of the employed CFD method for a store released from a weapon bay. In earlier work [17], the AGARD case [33] for external store release was used. Over all available data for store release from cavities, experiments performed at the Arnold Engineering Development Center (AEDC) [34] are at conditions closer to the present computations, and have been selected for validation.

The Mach number was 0.95, and the cavity was assumed to fly at 6096m. The Captive Trajectory System (CTS) was used. Using the standard atmosphere, the flight conditions were equivalent to a temperature of -24.6°C, a static pressure of 46619 Pa, and a density of 0.65 kg/m3. The full scale cavity was 4.57m long, 1.02m wide with L/D of 4.5. The employed store was 2.87m long, with four fins and canards in a cross configuration. The store had five degrees of freedom with rolling disabled. At carriage, the store CG was at
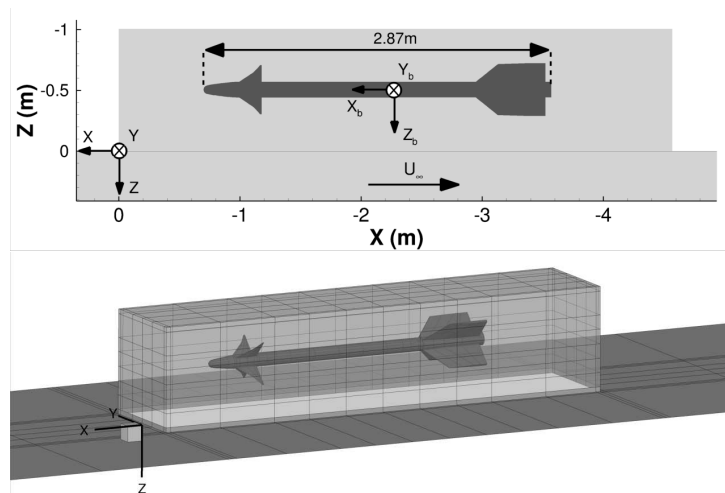
Figure 12: Geometry, cavity axis, and store at carriage position.

half cavity depth. After an ejector stroke where the store translated verti-
cally, the store was released with a full size downward velocity of 9.14m/s,
and a pitch, nose-down velocity of 57deg/s. The store release characteristics
are summarised in table 5. The wind tunnel Reynolds number based on the
scaled cavity length of 0.46m was $3.75.10^6$.

Characteristics	
Weight	88.5 kg
Centre of Gravity	1.5 m (aft of store nose)
Pitch Inertia (I_y)	61.8 $kg.m^2$
Yaw Inertia (I_z)	61.8 $kg.m^2$
Stroke Length	0.2 m
Stroke Velocity	9.14 m/s
Initial Pitch rate	57.3 deg/s

Table 5: Full-scale store and ejector characteristics[34].
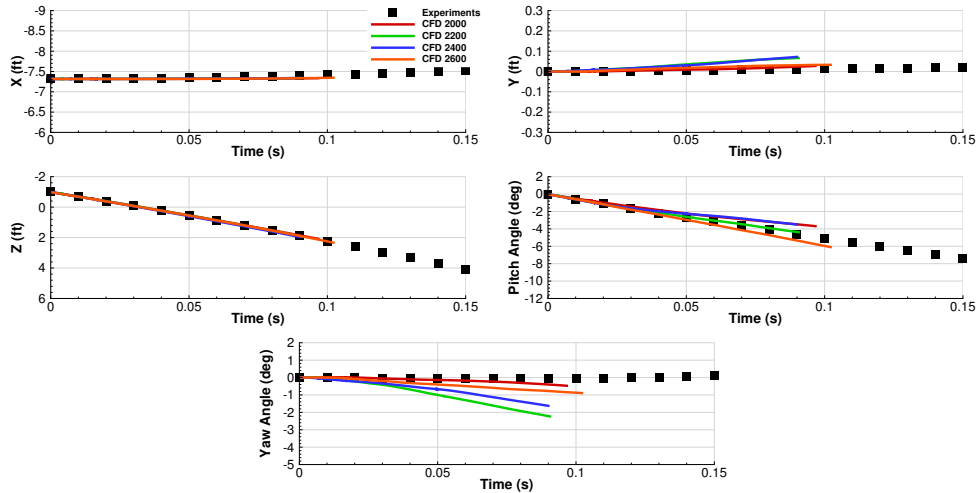
Figure 13: Store position during release.

Four releases are performed at different times, and the results are shown in figure 13 between HMB using SAS, Kim [35] using DES, and experiments. The displacements in the stream-wise, and span-wise directions are small, and less than two centimetres. The vertical displacement is mainly driven by gravity, and ejection characteristics, and no significant variability is seen in the computations for it. However, the store attitudes, show large variability in pitch and yaw, as also seen in reference [35].

4   Results and Discussion

4.1   Store Aeroelasticity in Clean Cavity

Simulations were carried out with the store at the carriage and at shear layer of the cavity without doors, and are summarised in table 6. At each store position, two computations were performed with rigid and elastic store body to determine if the fins are influenced by the body motion. In this section the carriage body modes were used since the store was fixed. 10 travel times takes in average 4 clock days on a 240 core computer.

Name	Store position	Fins structure	Body structure	Travel Time
Carriage fins	Carriage	Elastic	Rigid	41.0
Carriage fins and body	Carriage	Elastic	Elastic	77.2
Shear layer fins	Shear layer	Elastic	Rigid	42.0
Shear layer fins and body	Shear layer	Elastic	Elastic	88.2

Table 6: Computed aeroelastic cases

Figure 14 shows the sound pressure level (SPL) along the cavity ceiling mid-span with and without the store. In the following, the cavity modes are called M1 to M6. The clean cavity presents strong resonance up to the
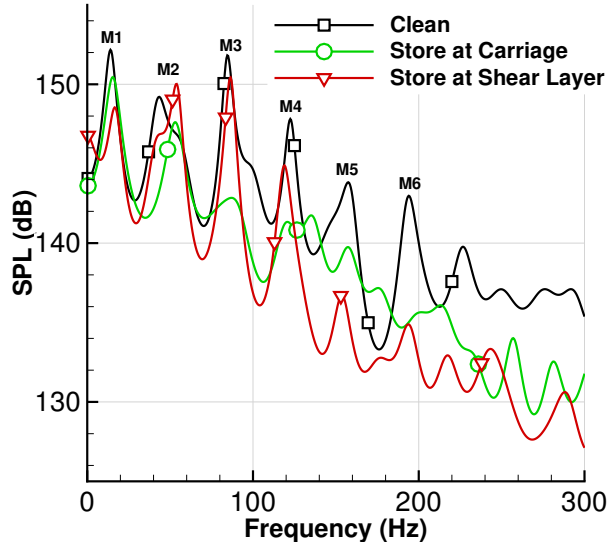
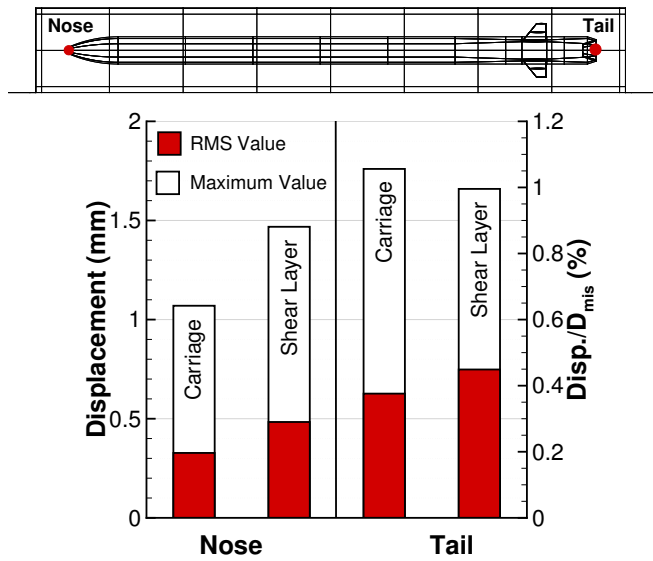Figure 14: SPL along the cavity ceiling mid-span.

Figure 15: Deformations of the body at carriage and shear layer.

27

sixth cavity mode. Adding the store at shear layer, reduces the broadband noise and the tonal amplitudes of modes 1, 4, 5 and 6. Moving the store at carriage, the noise decreases further with weaker tones. This is due to the blockage effect of the store that reduces the flow fluctuations inside the cavity.

Figure 15 shows the RMS and maximum displacements of the store body nose and tail at carriage and shear layer. Overall, the tail vibrates at larger amplitude as most of the cavity flow unsteadiness occurs at the aft of the cavity. Moving from carriage to shear layer position, the RMS deformations increase by 40%, and the maximum deformations reach 1.8mm. This corresponds to about 1% of the store diameter.
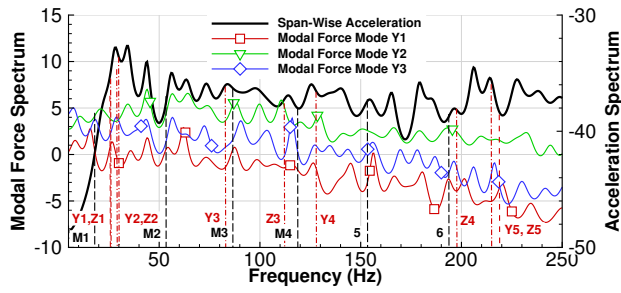
The span-wise and vertical accelerations of the body tail are shown in figure 16 at carriage and at shear layer. They are respectively shown with the modal forces of the modes Y_i and Z_i contributing to the deformation along the Y, and Z axes. The modal forces of modes above Z3 are not shown as they drive negligible deformations. Between carriage, and shear layer positions, the trends are similar, with an acceleration peak close to the structural modes Y1, Z1, Y2 and Z2, followed by a second weaker peak close to Z4, Y5, Z5. The body has a directional dependent response to the cavity flow. In the span-wise direction, the modal forces do not show strong peaks close to the cavity flow modes, and the body is only exited at its modal frequencies. On the other hand, the vertical modal forces exhibit peaks near the cavity modes. At carriage, the cavity modes M1 and M2 are visible in the modal forces and accelerations. At the shear layer position, there are stronger fluctuations, and all modal forces show peaks at the cavity modes M1 to M5, leading to significant acceleration peaks. The directionality of the acceleration is caused by the relatively symmetric cavity flow modes around the cavity mid-
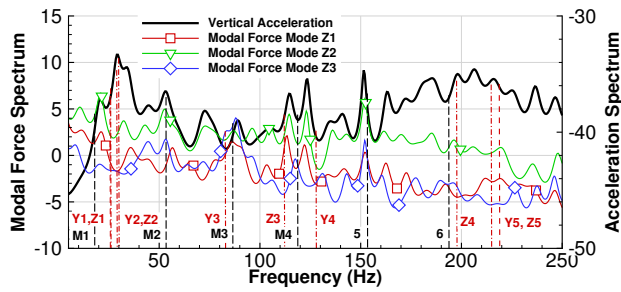
28
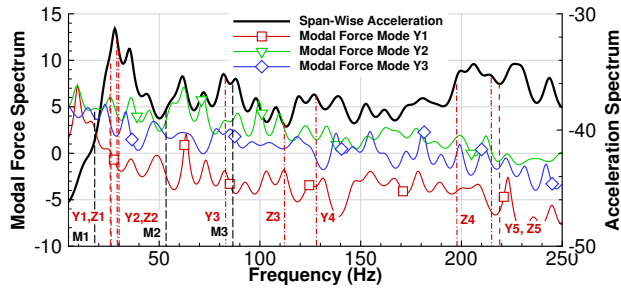
(a) Span-wise acceleration at carriage
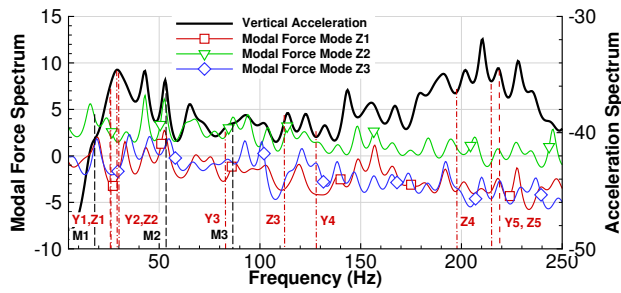
(b) Vertical acceleration at carriage

(c) Span-wise acceleration at shear layer

(d) Vertical acceleration at shear layer

Figure 16: Spectrum of body modal forces, and tail acceleration.

29

span, leading to weaker unsteady loads in the span-wise direction. When the store is at the shear layer, it is subjected to the strongest vertical loads due to the large differences between the cavity flow and the free-stream. The experiments in reference [4] show a similar behaviour with a smaller store model.

Figure 17 presents the RMS and maximum displacements of the trailing

(a) Fin 3   (b) Fin 4
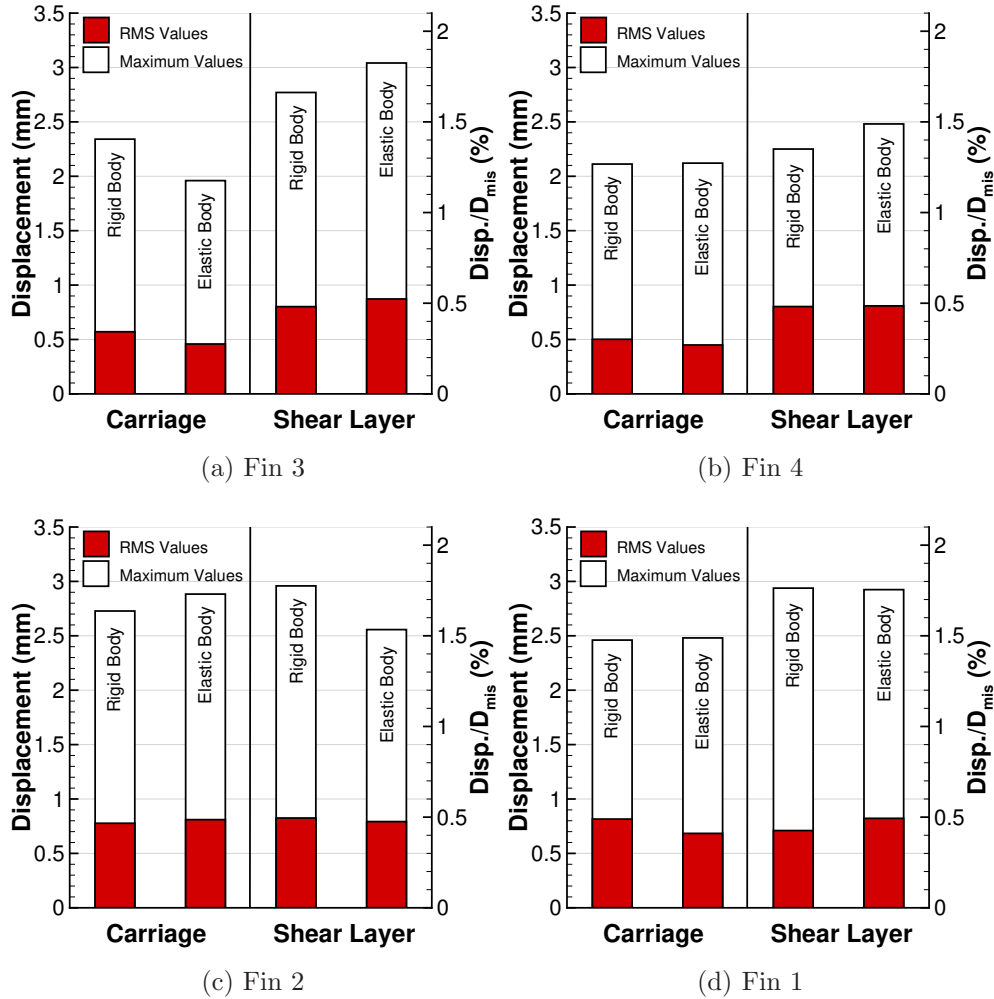
(c) Fin 2   (d) Fin 1

Figure 17: Fin trailing edge tip deformations (fin root reference frame)

edge tips of the fins at carriage and shear layer. Here, the displacements are shown in a reference frame attached to the fin root, and moving with the store body. The body elasticity has a small effect on the fins, because its deformations remain about 1% of the store diameter. However, fins 1 and 2 are close to the shear layer for both store positions, leading to similar RMS deformations of about 0.8mm. Moving closer to the shear layer, fins 3 and 4 on the upper side of the store are subject to an increase of 60% of their RMS displacement from 0.5 to 0.8mm. The maximum deformations reach values of about 3mm. In the earth axis, the RMS and maximum displacements respectively reach values of 1.0mm and 3.5mm.

At the trailing edge tip of fin 4, the acceleration spectra are compared between the cases with rigid and elastic bodies, in figure 18. The fin accelerations show a peak at the two first structural modes. This supports that the body elasticity has a small effect on the fin deformations with no visible influence of the body acceleration.

The spectra of the modal forces of the four fins are shown in figures 19a and 19b with the store at carriage and shear layer. The modal forces of modes F3 and F4 are not shown here as they lead to negligible deformations. Overall, the modal forces are not influenced by the cavity modes. At carriage, fins 1 and 2, are closer to the shear layer than fins 3 and 4, and are exposed to stronger flow fluctuations. At the shear layer, where all the fins are exposed to the flow turbulence, they show similar modal forces. The response of the fins to the modal force shown in figures 19c and 19d, are also characterised by changes in the high frequency amplitudes regarding the store position. This shows that the fin deformations are mainly driven by the high frequency broadband noise.
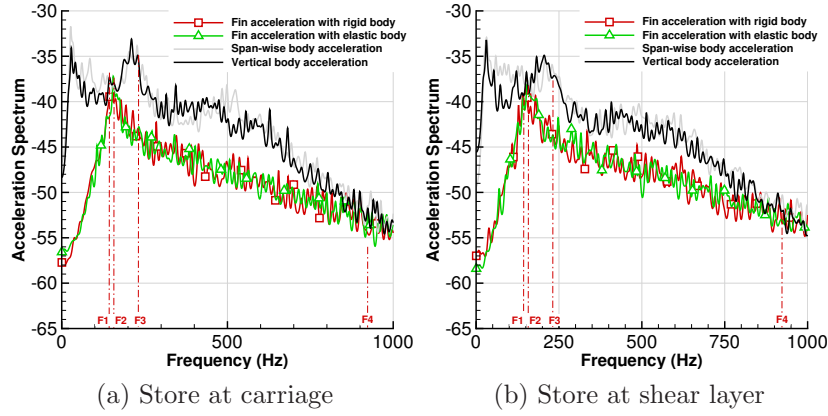
(a) Store at carriage (b) Store at shear layer

Figure 18: Fin 4 acceleration spectra with and without body aeroelastics.

(a) Modal force - Carriage (b) Modal force - Shear layer

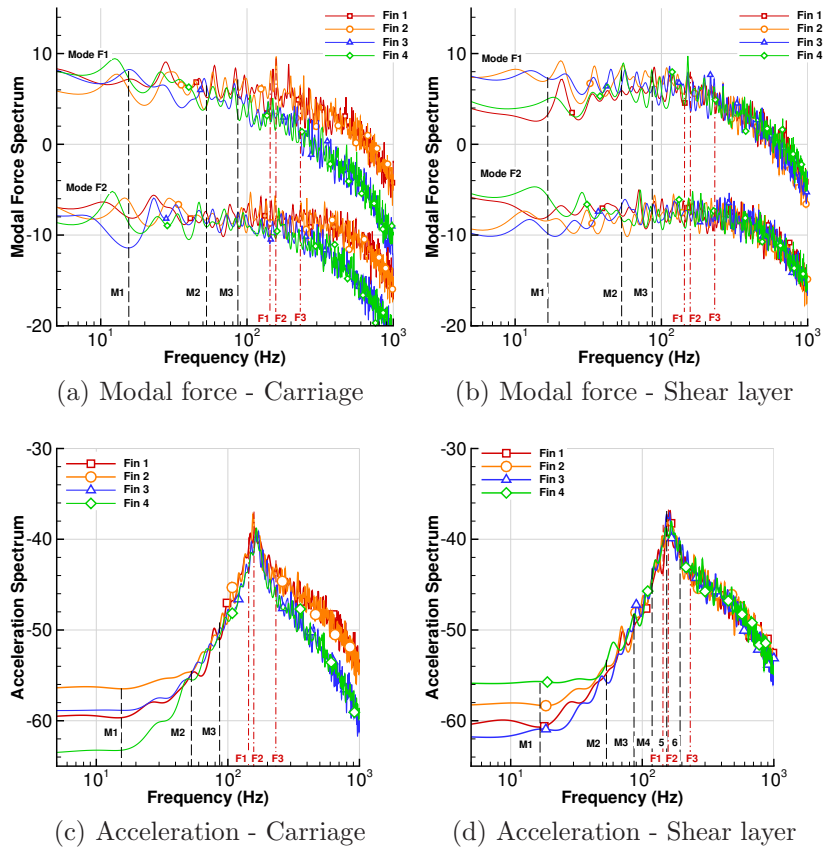(c) Acceleration - Carriage (d) Acceleration - Shear layer

Figure 19: Fin modal forces spectra, and trailing edge tip acceleration of the fin.

4.2 Store Aeroelasticity with Doors

This section presents results of computations including an aeroelastic store placed at carriage with doors. Static doors are held at 20, 45, 90 and 110 degrees, and are dynamically moving from 0 to 110 degrees at 220deg/s. The computations are also compared with the results of reference [18] that presents similar computations, without the store. Table 7 summarises the computed cases.

Figure 20 shows time averaged Mach number field and Linear Integral Convolution (LIC) [36] at the cavity mid-span for the dynamic opening with and without store. The dynamic cases are averaged over windows of 10 degrees centred in the investigated angle. The static cases are averaged over the total time signal available. The case without store shows three steps

Name	Angle (deg)	Door Velocity (deg/s)	Travel Time
Doors with Aeroelastic Store at Carriage			
Static & Store 20deg	20	0	19.6
Static & Store 45deg	45	0	21.6
Static & Store 90deg	90	0	19.2
Static & Store 110deg	110	0	19.1
Medium & Store	110	220	40.0
Doors without Store (Reference [18])			
Static 20deg	20	0	22.0
Static 45deg	45	0	20.0
Static 90deg	90	0	20.0
Static 110deg	110	0	38.0
Medium	110	220	82.0

Table 7: Computed cases with doors

during the cavity flow establishment as described in reference [18]. As soon, as the door opening begins, a jet appears between the doors and the cavity front lip (Figure 20a), producing disturbances at the cavity front. When

(a) No Store - 5deg

(b) Store - 5deg

(c) No Store - 20deg

(d) Store - 20deg

(e) No Store - 35deg

(f) Store - 35deg

(g) No Store - 45deg

(h) Store - 45deg
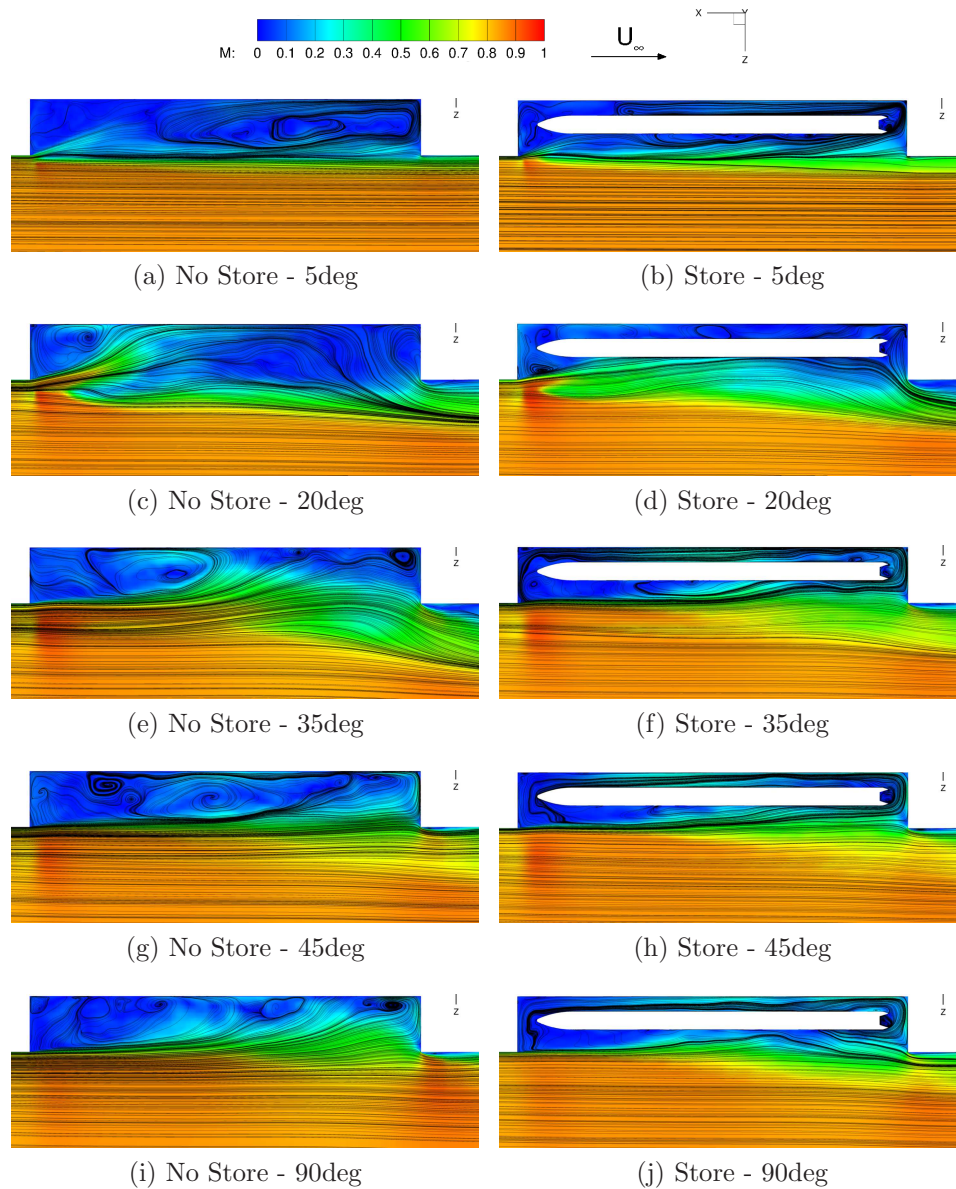
(i) No Store - 90deg

(j) Store - 90deg

Figure 20: Mach number and LIC at mid-span during door opening.

reaching the ceiling, the flow resembles a closed cavity configuration (Figure 20c) but rapidly switches to a transitional flow (Figure 20e). Finally, the jet detaches from the ceiling, and an open cavity flow establishes with the shear layer spanning the cavity length (Figure 20g). With the store at carriage, the flow also establishes with closed, transitional, and open flow steps. However, the store shields a part of the cavity ceiling, and the jet hits the store while the flow evolves.

The loads on the cavity walls are presented in figure 21 for the cases with and without store. The signals of the dynamic cases are averaged over

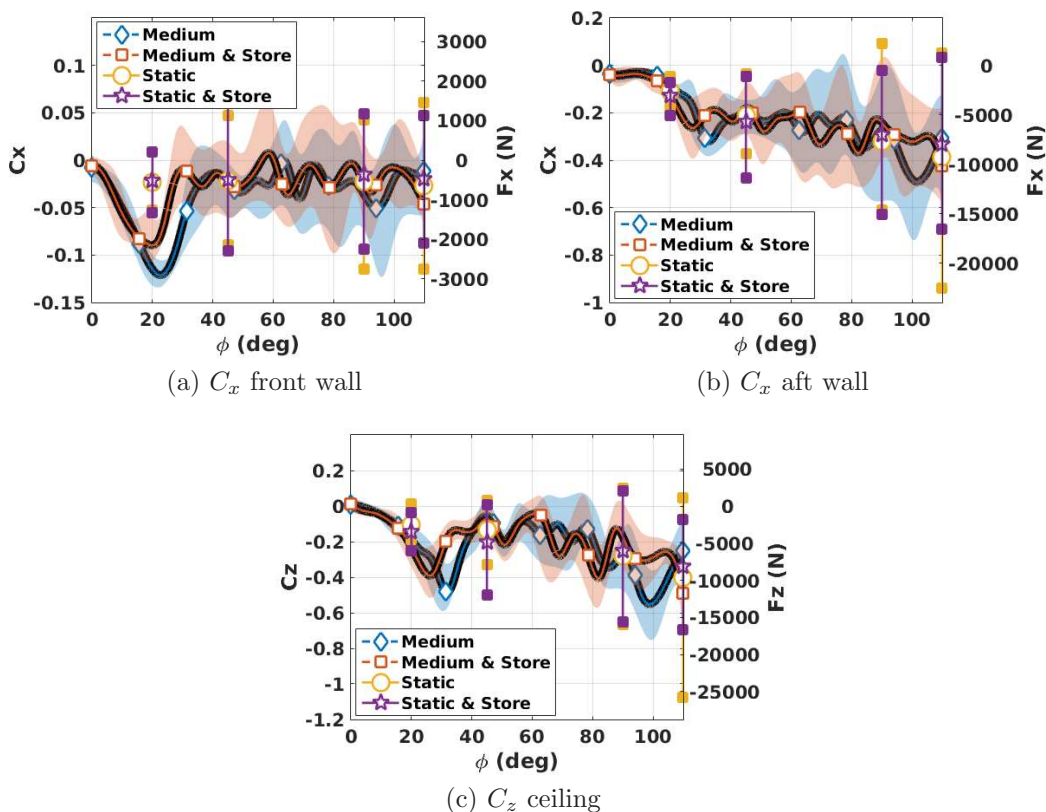(a) C_x front wall (b) C_x aft wall

(c) C_z ceiling

Figure 21: Force on the cavity walls during medium speed door opening.

windows of 1.6 travel times, and the min and max of the signal over the window are also computed and shown as shaded envelope. This window width filters the frequencies above 50Hz for better readability of the plot, and for the static cases, the full time signal is used. The dynamic case shows a peak around 20 degrees when the jet interacts with the cavity (Figure 20c), and the loads approach the static values when the open cavity flow is established. Adding the store at carriage, shields the cavity walls (Figure 20d), and alleviates peak loads due to the jet, while, after the flow transitions to an open configuration, the store does not influence the wall loads. The store loads (Figure 22) show small differences between static and dynamic cases during the transition at about 30 degrees opening as the jet affects only a small part of the store front. After transition (see figure 22 at $\phi > 50$ degrees), the store load fluctuations increase reaching values close to one of the static door case as the flow develops.

In figure 23, the store deformations are shown for static door cases with and without doors (left column), and for dynamic cases with doors (right column). The RMS values are computed for the dynamic cases over windows of 1.6 travel times, and the envelope is represented in figure 21. Adding the fully opened doors to the cavity, the RMS displacements are unchanged (see red bars in figures 23a and 23c), because of a small effect of the doors at the mid-span of the cavity, as also shown in reference [18]. During the dynamic opening, the fin displacements are increasing with the door angle (Figure 23d), but not reaching larger values than the fully opened case. However, the body shows a different behaviour, with a peak deformation at the nose where the jet hits the store at about 20 degrees (Figure 23b), with larger RMS values compared to the static door cases. Nevertheless, the maximum values are smaller than for the static cases. The body tail behaves like the
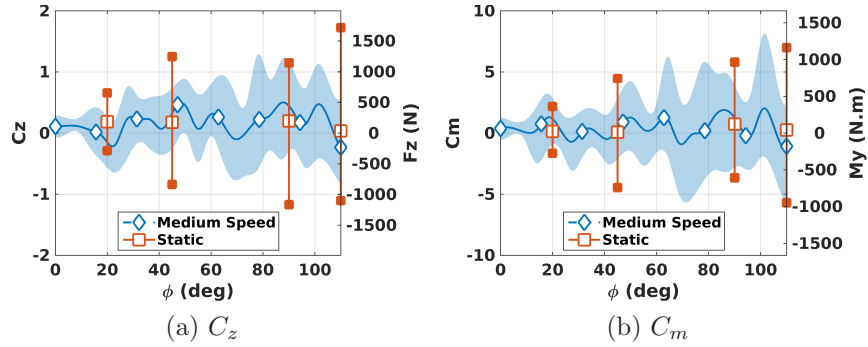
(a) C_z (b) C_m

Figure 22: Force on the store during medium speed door opening.

(a) Static - Store body (b) Dynamic - Store body

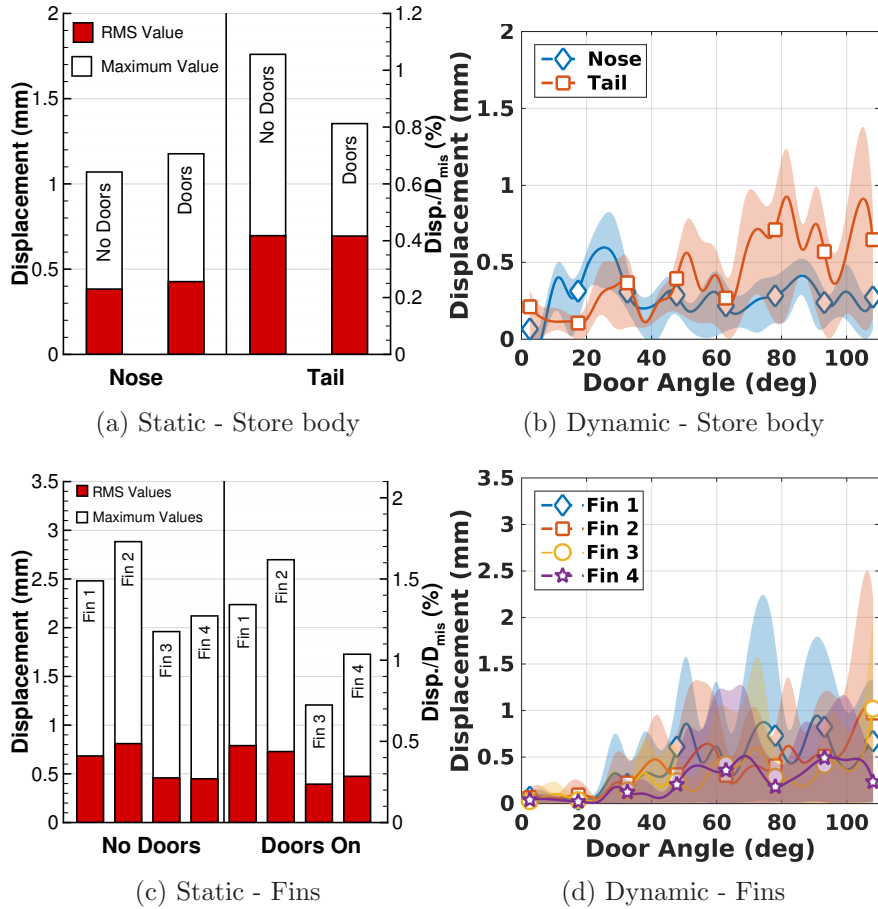(c) Static - Fins (d) Dynamic - Fins

Figure 23: Deformation of the store during medium speed door opening.

fins, because it is not directly impacted by the jet during transition.

This section shows that the door opening is not a critical case for the present cavity/store combination, as the structural deformations are of the same order of magnitude compared to the fully established flow.

4.3 Aeroelastic Store Release

This section is the continuation of the work presented in reference [17] where twenty store release simulations were performed with the store modelled as rigid. This paper goes further adding the aeroelasticity to the complete store. The following computations do not include bay doors. See section 4.4 for case with doors.

4.3.1 Store Release Process

The store release includes three phases. At *carriage* (Z/D=-0.5), the store is fixed and computed using aeroelastics while the flow is allowed to develop. Then, during the *stroke phase*, the store is pushed towards the cavity opening at a vertical velocity of 5m/s, with other degrees of freedom set to zero. This phase ends when the stroke length of 0.129m is reached. Finally, the store is free to move under the aerodynamic forces. At carriage, and during the stroke phase, the store is fixed to the ejection system (not included in the CFD geometry), and the carriage modes are activated. At the end of the stroke, the store detaches from the ejection mechanism. To ensure continuity of the computation, the carriage modes are still active with their forces $f_m^s(t)$ set to zero to stop their excitation. At the same time, the free air structural modes are activated. Figure 24 shows the deformations at the body tail due to both sets of modes during the release HS10000. Computations carried out
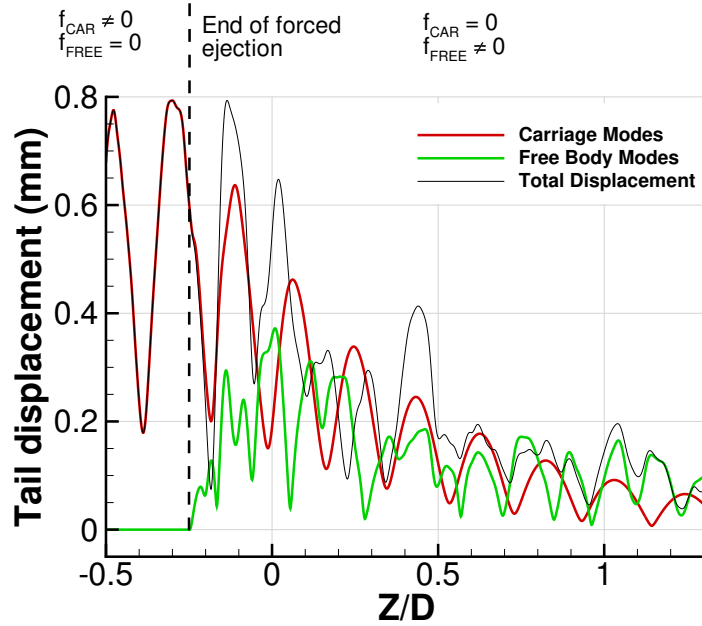
Figure 24: Tail displacement decomposition during store release HS10000.

for different release times are shown here, and are summarised in table 8.

4.3.2 Results and Discussion

Statistical convergence is tested using the maximum of the normalised difference between the average of n+1, and n trajectories defined as in reference [17]:

$$\Delta_\mu = \frac{max|\mu(t, n + 1) - \mu(t, n)|}{W_e} \tag{20}$$

with $\mu(t, n)$ the average of n trajectories, where t covers the complete time of simulation. The envelope of the trajectory is defined as the maximum difference between minimum, and maximum over all releases and all store vertical positions. W_e is the largest envelope width over all positions. A trajectory

39

	Stroke Start	
ID	**Travel Time**	**Time (s)**
HS9300	93	0.93
HS9600	96	0.99
HS9900	99	1.00
HS10000	100	1.02
HS10200	102	1.04
HS10500	105	1.08
HS11100	111	1.16
HS11400	114	1.19
HS11700	117	1.23
HS13800	138	1.49
HS14000	140	1.52
HS14200	142	1.54
HS16300	163	1.81
HS16500	165	1.83
HS16700	167	1.86

Table 8: List of carried elastic releases.

component was considered as converged if the difference (Δ_μ) between two consecutive averages was less than 5%. The number of releases to converge the statistics depends on the order of the trajectories. To minimise this effect, Δ_μ was computed for 100.000 random trajectory permutations. For each permutation, the number of releases required to converge the statistics was computed, and the cumulative plot in figure 25a indicates the number of converged permutations with respect to the number of releases included in the mean. The statistics are always converged after 13 releases. Conse-
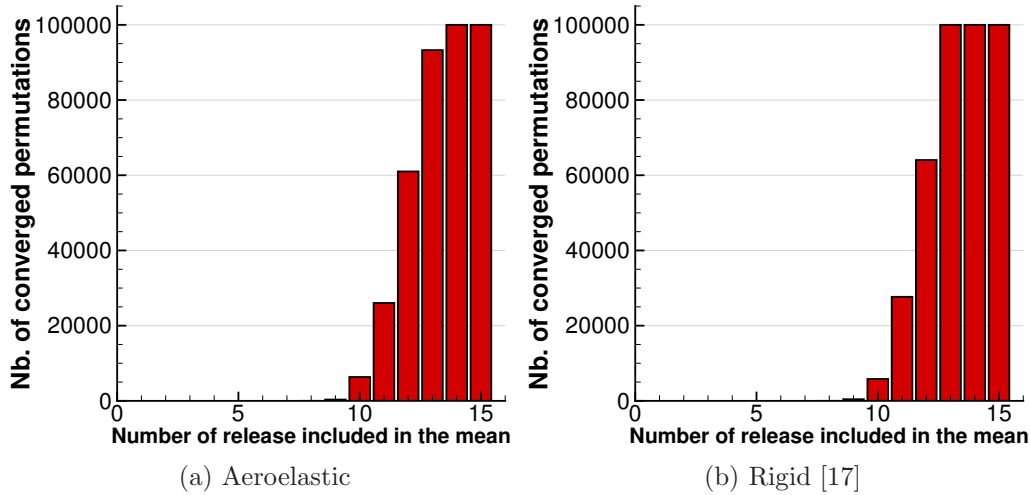
(a) Aeroelastic   (b) Rigid [17]

Figure 25: Converged release permutations number in function of the number of releases.

quently, this average is seen as converged for this case, and the results can now be used to compute a mean flow. Aeroelastic results are compared to 15 rigid store cases with half stroke from reference [17]. Figure 25b shows the convergence for the rigid cases, and there is small differences with the elastic cases.

Figure 26 shows the store trajectory for elastic and rigid releases. The average over all releases is shown as solid lines, and the envelope as shaded area. Overall, the averaged loads are unchanged by the store aeroelasticity because the deformations are not large enough to lead to any significant flow modification. The variability in roll is evident in the results of figure 26, and the difference between rigid and elastic cases are more pronounced. However, the difference is less than a degree, and this will be further reduced, running more releases, as this component is driven by small turbulence structures [17]. The amplitude of the roll angle variability is, however, of similar size

(a) C_z : Vertical Force (b) w : Vertical Velocity

(c) C_l : Rolling Moment (d) C_m : Pitching Moment (e) C_n : Yawing Moment

(f) ϕ : Rolling Angle (g) θ : Pitching Angle (h) ψ : Yawing Angle
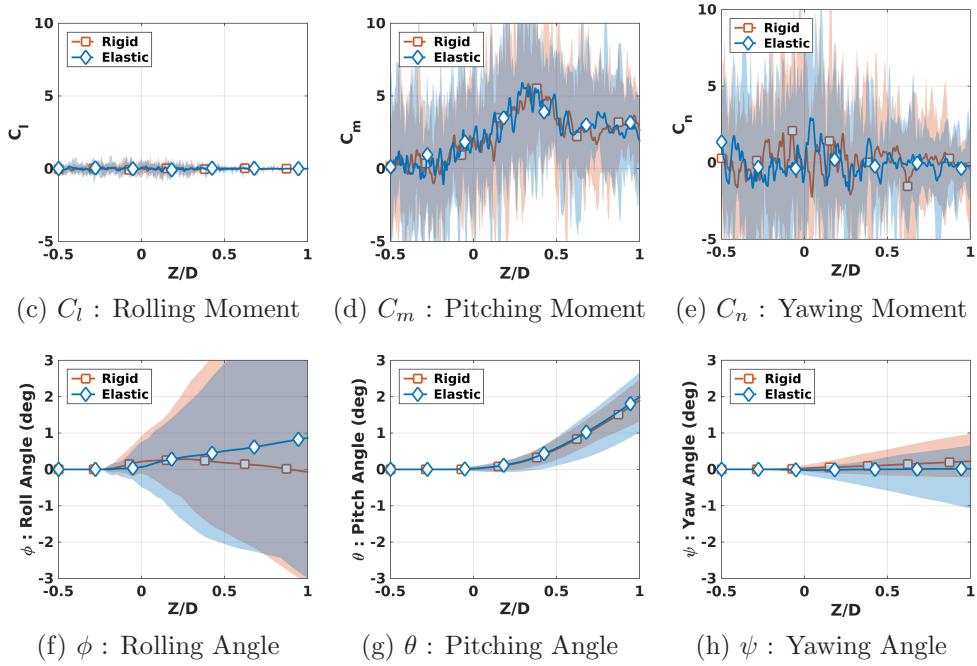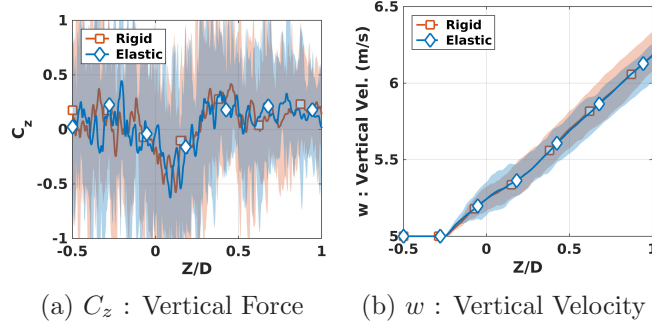
Figure 26: Average and envelope (peak to peak) of store trajectory during release.

between rigid and aeroelastic.

The store deformations are shown in figure 27 for the body and the trailing edge tip of the fins during the aeroelastic release. The average over all releases is shown as solid lines, and the standard deviation as shaded area. As the store clears the cavity, its tail leaves the influence of the cavity flow
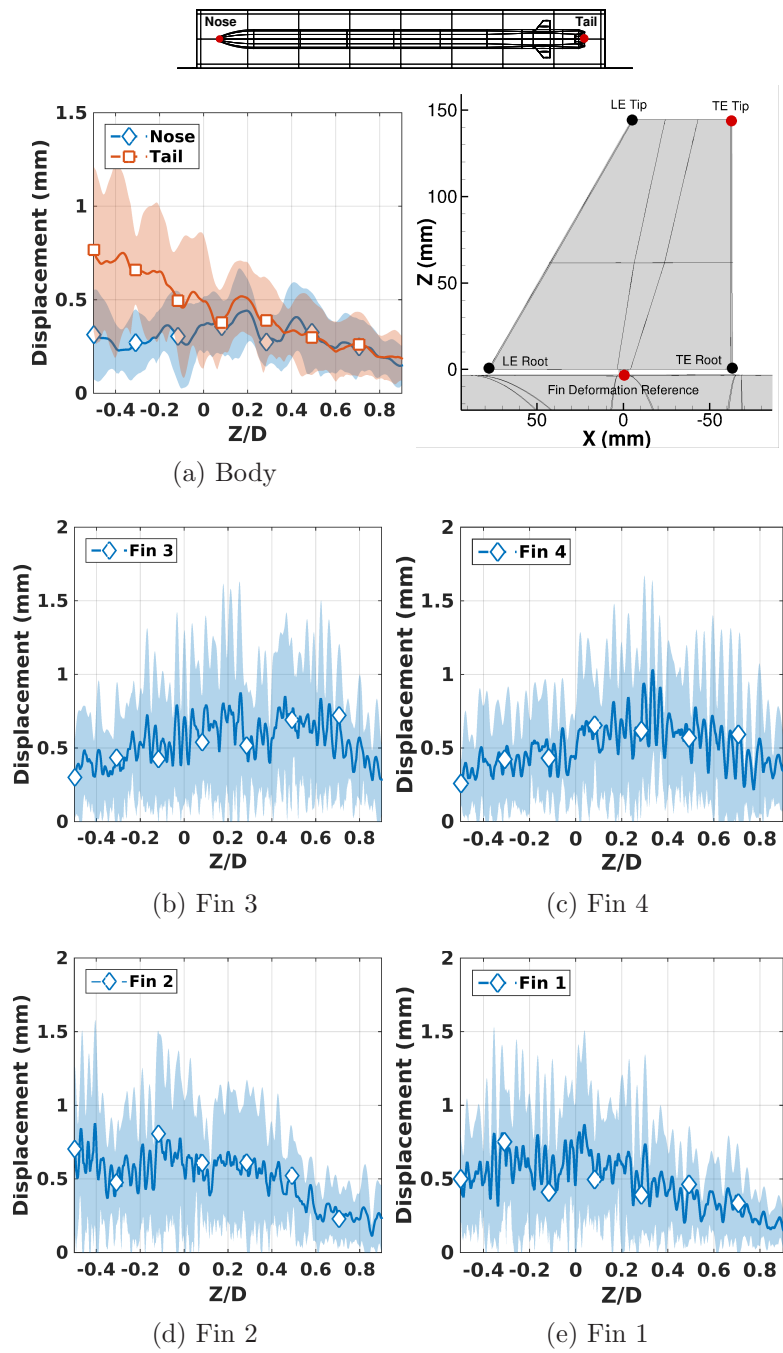
42

Figure 27: Average and standard deviation of body, and trailing edge tip deformations.

fluctuations at the cavity aft, and its structural deformations become smaller. On the other hand, the store nose reaches a peak of deformation when it interacts with the shear layer at Z/D=0.2. Further away from the cavity, the store reaches the free-stream, and the deformations are getting closer to zero.

The fins behave differently during the release. Fins 1 and 2 are subject to larger deformations when the store is inside the cavity, as they are directly exposed to the turbulent shear layer. Moving outside the cavity, the fins rapidly leave the high pressure fluctuations, and their deformations become smaller. Fins 3 and 4 present a peak of deformation when the store is around

| ID | Stroke Start | |
	Travel Time	Time (s)
DHS3180	32	0.16
DHS3300	33	0.18
DHS3730	37	0.23
DHS3900	39	0.25
DHS4100	41	0.28
DHS4300	43	0.30
DHS4520	45	0.33
DHS4700	47	0.35
DHS4900	49	0.38
DHS5100	51	0.40
DHS5930	59	0.51
DHS6100	61	0.53
DHS6300	63	0.55
DHS6500	65	0.58
DHS6700	67	0.60

Table 9: List of carried elastic releases with doors.

Z/D=0.4. At this point, the fins are in contact with the turbulent shear layer which is more active than for the fully established cavity flow, due to the interaction between the store nose and the shear layer [17].

4.4 Aeroelastic Store Releases with Static Doors

This section describes the most realistic release configuration, where the store is aeroelastic, and the doors are present and open at 110 degrees. The aeroelastic model including carriage, and free flight modes is the same as used in section 4.3, and only half stroke releases are simulated. Twelve releases were computed at different stroke start times, and are summarised table 9.

Figure 28 shows the number of converged permutations as function of the number of releases included in the mean, with a criterion of 5% using equation 20. This is the same criterion as for the case of releases with aeroelasticity, and no doors. The statistics always converge after 13 releases. Consequently, this average is seen as converged for this case, and the results can now be
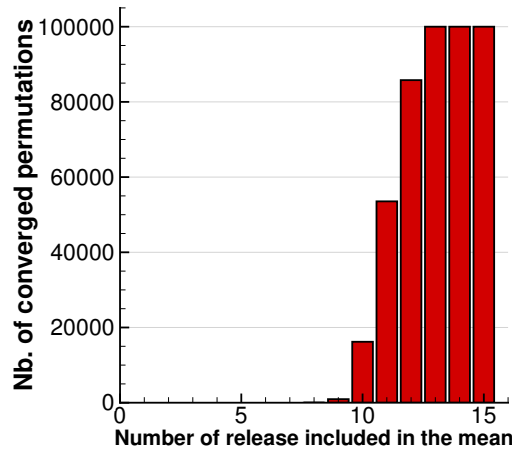

Figure 28: Converged release permutations number in function of the number of releases.

(a) C_z : Vertical Force (b) w : Vertical Velocity

(c) C_l : Rolling Moment (d) C_m : Pitching Moment (e) C_n : Yawing Moment

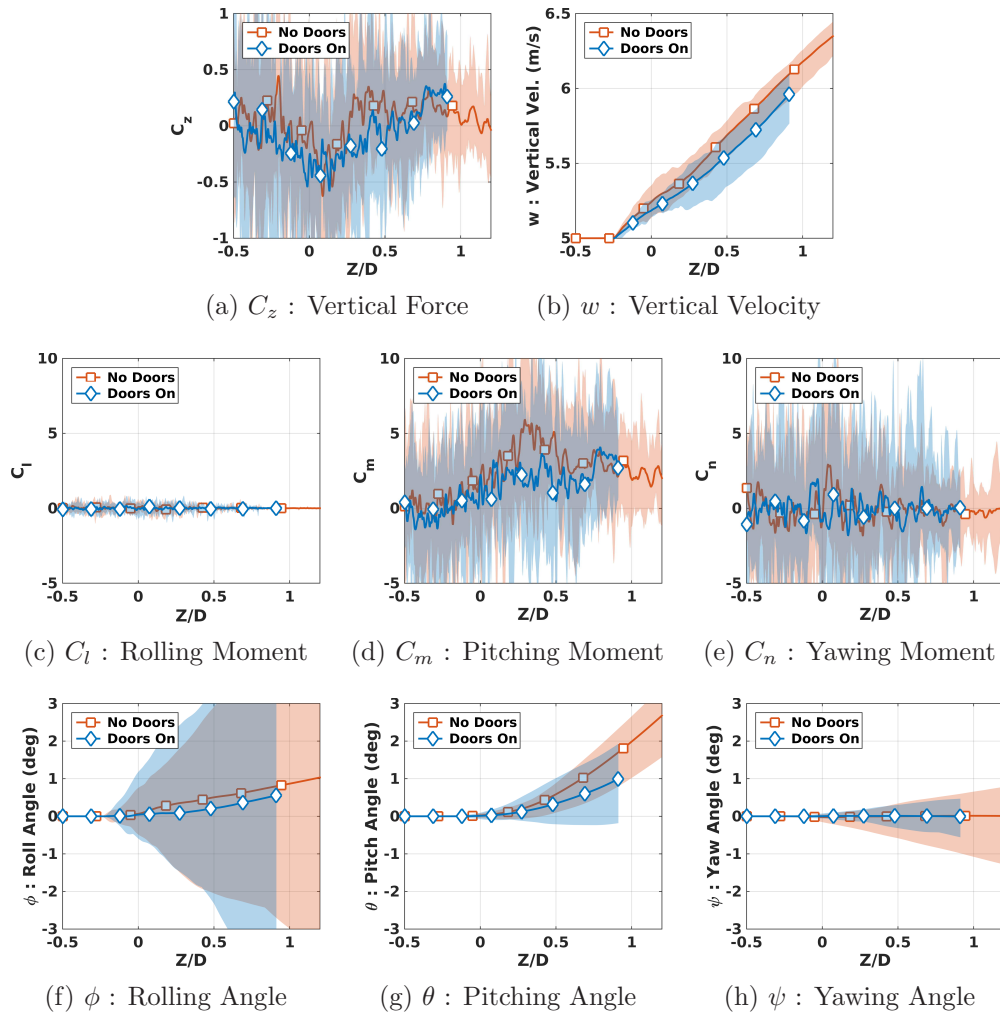(f) ϕ : Rolling Angle (g) θ : Pitching Angle (h) ψ : Yawing Angle

Figure 29: Average, and envelope (peak to peak) of store trajectory during aeroelastic releases.

used to compute a mean flow and make comparisons between doors and no door cases.

Figure 29 shows the trajectory of the aeroelastic store for the doors, and no doors cases, averaged from all available releases. Also, the envelope computed from all the releases is shown as shaded area. The vertical velocity, and

the pitch angle are slightly smaller with the doors, while all other components are very similar.

Figure 30 shows the the C_p at the mid-span of the cavity averaged from all available releases without and with doors (respectively left and right columns). Overall, the aft cavity region of high pressure (showing in orange colour) is reduced with the doors on. This weaker pressure rise at the aft wall results in smaller pitch angle for the store.

Figure 31 shows the deformation of the store on the body, and the fins at the tip of their tailing edge. The average computed using all the available releases is shown in solid lines, and the standard deviation is shown as shaded area. Differences between the two cases appear when the store travels outside of the cavity. The nose andd the tail are subject to twice larger deformation for $Z/D > 0.4$, and the standard deviation is also wider adding the doors. The fins are also subject to larger vibrations outside the cavity with doors, both in amplitude and mean value, mainly visible for fin 4. This is due to the doors that channel the pressure fluctuations outside the cavity, as can be seen in figure 32, that shows the OASPL at X/L=0.85, for different store positions. Further realism could be achieved adding aeroelasticity to the doors, which vibrations may change the noise directivity.

This study shows that important features like doors should be modelled, to correctly capture the complete store interaction with the cavity flow. With the doors held at 110 degrees, the flow in the cavity is very close to the case without doors. However, the doors at 110 degrees still had a small effect on the store pitch angle, and vertical velocity. The next step is to take into account complex internal cavity geometry, and the presence of multiple stores since small differences inside the cavity can impact the flow significantly.
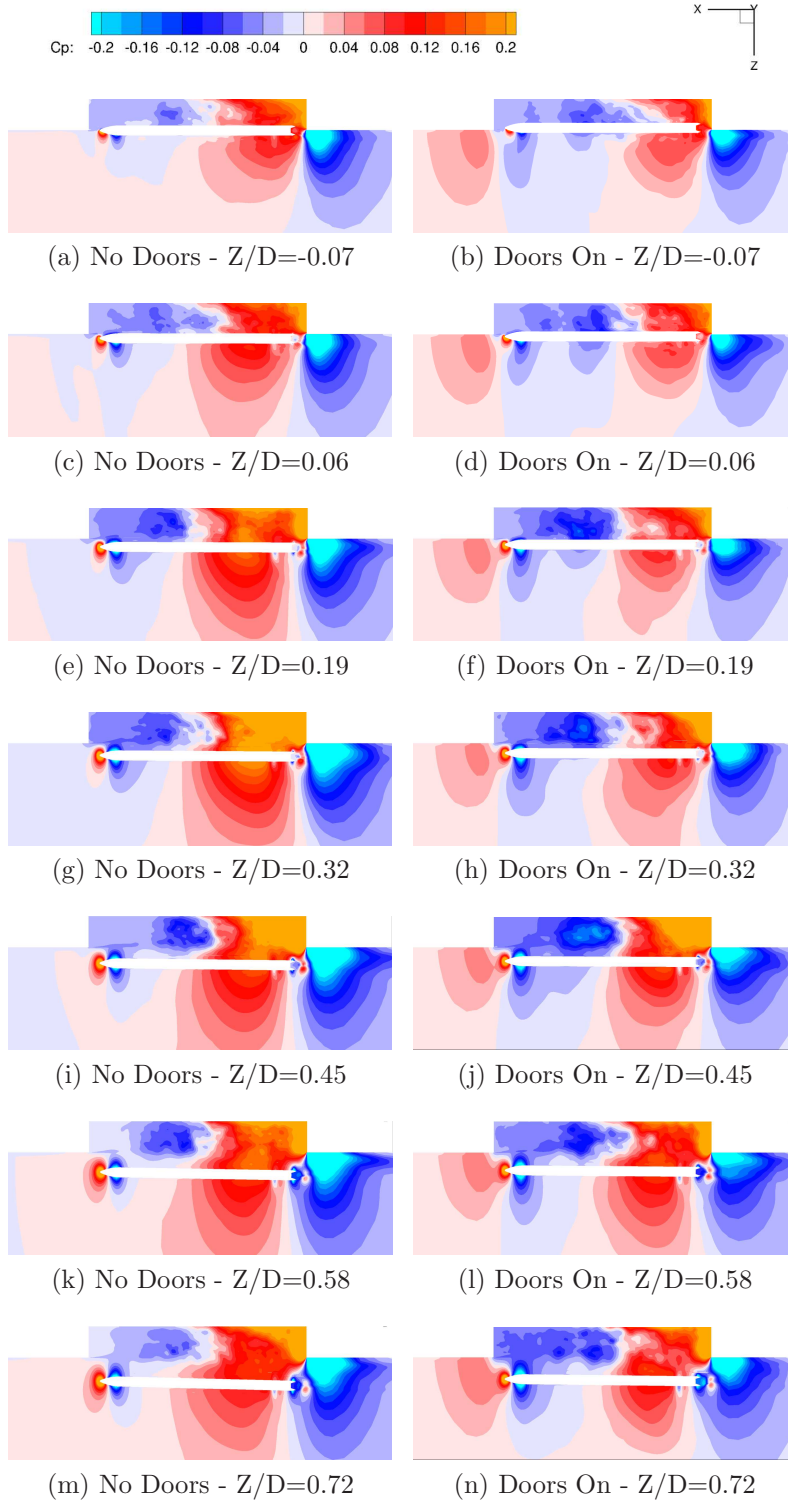
Figure 30: C_p field at the cavity mid-span averaged from all available releases.
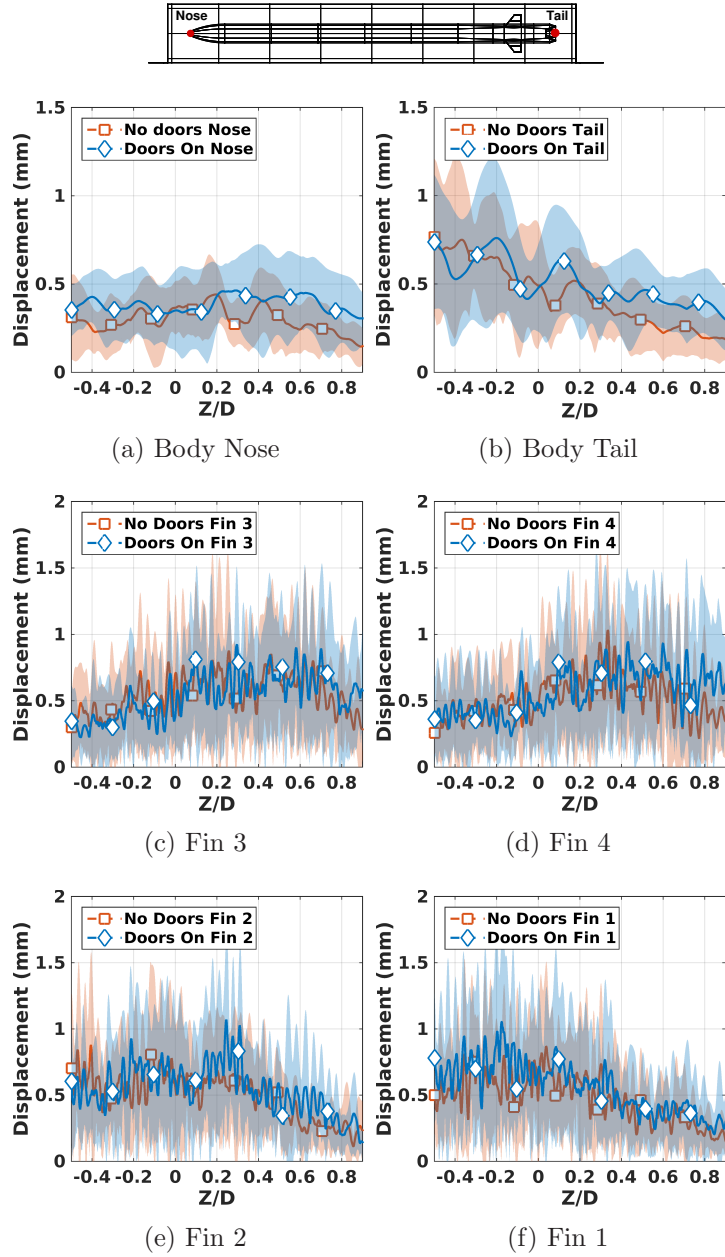
Figure 31: Average and standard deviation of body, and trailing edge tip deformations.
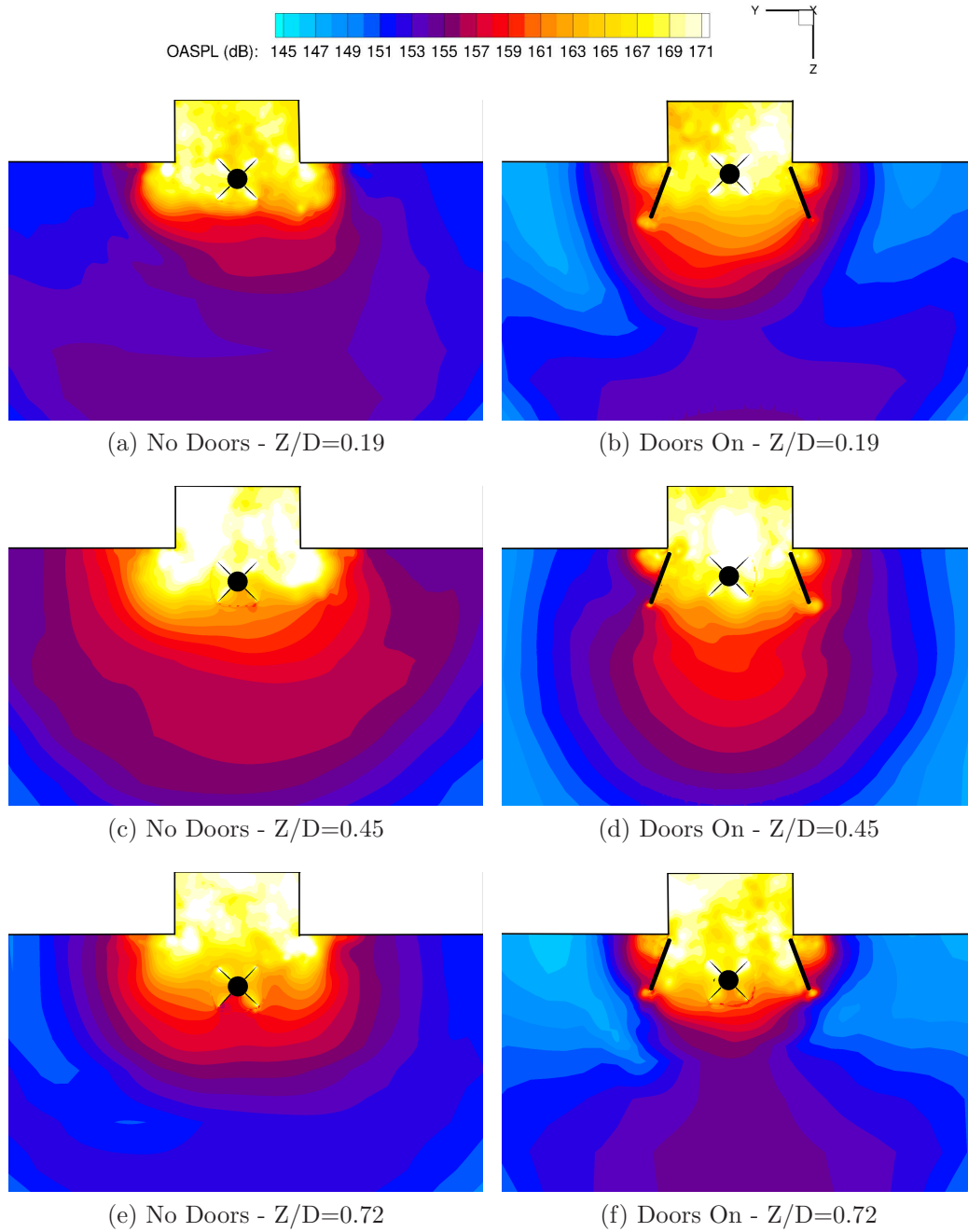
(a) No Doors - Z/D=0.19

(b) Doors On - Z/D=0.19

(c) No Doors - Z/D=0.45

(d) Doors On - Z/D=0.45

(e) No Doors - Z/D=0.72

(f) Doors On - Z/D=0.72

Figure 32: OASPL field at X/L=0.85 averaged using all available releases.

5 Conclusions

This paper presented a set of calculations involving door opening, cavity flow development, and store release. The store elasticity was modelled to quantify the structural deformations occurring during the weapon bay operation. The tonal fluctuations excited the store body, while the fins were more influenced by the broadband part of the flow fluctuations. Overall, maximum store deformations were of about 2% of the store diameter. This is the first time that such effects are quantified for store releases. The store trajectory variability was similar for cases with or without aeroelasticity. For the case at hand, the aeroelasticity effects were secondary, with cavity flow effects dominating the release. The present results suggest that the proposed method is efficient, and can be used with current generation computers for initial investigations of store clearance before flight testing.

References

[1] Rossiter, J. E., "Wind Tunnel Experiments on the Flow Over Rectangular Cavities at Subsonic and Transonic Speeds," Technical Report 64037, Royal Aircraft Establishment, Bedford, UK, October 1964.

[2] Loupy, G. and Barakos, G., "Acoustic Field Around a Transonic Cavity Flow," *International Journal of AeroAcoustics*, Vol. 16, No. 6, 2017,

doi:10.1177/1475472X17730459.

[3] Probst, Z., Reeder, M., Johnson, R., and Grove, J., "Flight-Test Experiments on Cavity Flow in an SUU-41 Pod," *Journal of Aircraft*, 2017, doi:10.2514/1.C034203.

[4] Wagner, J., Casper, K., Beresh, S., Hunter, P., Spillers, R., Henfling, J., and Mayes, R., "Fluid-structure interactions in compressible cavity flows," *Physics of Fluids*, Vol. 27, No. 6, 2015.

[5] Wagner, J., Casper, K., Beresh, S., Hunter, P., Spillers, R., and Henfling, J., "Response of a store with tunable natural frequencies in compressible cavity flow," *Journal of Aircraft*, Vol. 53, No. 4, 2016, pp. 2351–2360.

[6] Casper, K., Wagner, J., Beresh, S., Spillers, R., and Henfling, J., "Study of Fluid-Structure Interactions on a Tunable Store in Complex Cavity Flow," *Proceedings of the 47th AIAA Fluid Dynamics Conference*, Paper No. AIAA 2017-3125, American Institute of Aeronautics and Astronautics Inc, Denver, Colorado, United states, 2017, doi:10.2514/6.2017-3125.

[7] Arunajatesan, S., Bharadwaj, M., Riley, W. C., and Ross, M., "One-Way Coupled Fluid Structure Simulations of Stores in Weapons Bays," *Proceedings of the 51st AIAA Aerospace Sciences Meeting including the New Horizons Forum and Aerospace Exposition*, Grapevine, Texas, USA, 7-10 January 2013, doi:10.2514/6.2013-665.

[8] Babu, S., Loupy, G., Dehaeze, F., Barakos, G., and Taylor, N., "Aeroelastic simulations of stores in weapon bays using Detached-Eddy Simulation," *Journal of Fluids and Structures*, Vol. 66, October 2016, pp. 207–228, doi:10.1016/j.jfluidstructs.2016.07.014.

[9] Barakos, G., Steijl, R., Badcock, K., and Brocklehurst, A., "Development of CFD capability for full helicopter engineering analysis," *Proceedings of the 31th European Rotorcraft Forum - 13-15 Sep 2005*, Florence, Italy 2005.

[10] Steijl, R., Barakos, G. N., and Badcock, K., "A framework for CFD analysis of helicopter rotors in hover and forward flight," *International Journal for Numerical Methods in Fluids*, Vol. 51, No. 8, 2006, pp. 819–847, doi: 10.1002/d.1086.

[11] Lawson, S. J., Steijl, R., Woodgate, M., and Barakos, G. N., "High performance computing for challenging problems in computational fluid dynamics," *Progress in Aerospace Sciences*, Vol. 52, No. 1, 2012, pp. 19–29, doi: 10.1016/j.paerosci.2012.03.004.

[12] Babu, S., Zografakis, G., Barakos, G. N., and Kusyumov, A., "Evaluation of scale-adaptive simulation for transonic cavity flows." *International Journal of Engineering Systems Modelling and Simulation*, Vol. 8, No. 2, 2016, pp. 106–124, doi:10.1504/IJESMS.2016.075510.

[13] Jarkowski, M., Woodgate, M., Barakos, G., and Rokicki, J., "Towards Consistent Hybrid Overset Mesh Methods for Rotorcraft CFD," *International Journal for Numerical Methods in Fluids*, Vol. 74, No. 8, 2014, pp. 543–576, doi:10.1002/fld.3861.

[14] Loupy, G. and Barakos, G., "Processing and Analysis Methods for Transonic Cavity Flow," *Physics of Fluids*, Vol. 29, No. 16, 2017, doi:10.1063/1.4995461.

[15] Barakos, G., Lawson, S., Steijl, R., and Nayyar, P., "Numerical Simulations of High–Speed Turbulent Cavity Flows," *Flow, Turbu-*

lence and Combustion, Vol. 83, No. 4, December 2009, pp. 569–585, doi:10.1007/s10494-009-9207-1.

[16] Menter, F. and Egorov, Y., "The Scale-Adaptive Simulation Method for Unsteady Turbulent Flow Predictions. Part 1: Theory and Model Description," *Flow, Turbulence and Combustion*, Vol. 85, No. 1, 2010, pp. 113–138, doi:10.1007/s10494-010-9264-5.

[17] Loupy, G., Barakos, G., and Taylor, N., "Assessment of Store Release Variability from Weapon Bay using Scale Adaptive Simulation," *AIAA Journal*, 2017, doi:10.2514/1.J056485.

[18] Loupy, G., Barakos, G., and Taylor, N., "Cavity Flow Over a Transonic Weapon Bay During Door Operation," *Journal of Aircraft*, 2017, doi:10.2514/1.C03344.

[19] *Real Eigenvalue Analysis*, *NX Nastran Basic Dynamic Analysis Users Guide*, Siemens Product Lifecycle Management Software Inc, 2008, pp. 3–1 – 3–18.

[20] Ho, N., "Finding optimal rotation and translation between corresponding 3D points," http://nghiaho.com/, Last accessed 9th November 2017.

[21] Shepard, D., "A Two-dimensional Interpolation Function for Irregularly-spaced Data," *Proceedings of the 1968 23rd ACM National Conference*, New York, NY, USA, 1968, pp. 517 – 524, doi:10.1145/800186.810616.

[22] Biava, M. and Barakos, G. N., "Optimisation of Ducted Propellers for Hybrid Air Vehicles Using High-Fidelity CFD," *The Aeronautical Journal*, Vol. 120, No. 1232, 2016, pp. 16321657, doi:10.1017/aer.2016.78.

[23] R.J.Renka, "Multivariate Interpolation of Large Sets of Scattered Data," *ACM Trans. Math. Softw.*, 1988, pp. 139 – 148, doi:10.1145/45054.45055.

[24] Bonet, J. and Peraire, J., "An alternating digital tree (ADT) algorithm for 3D geometric searching and intersection problems," *International Journal for Numerical Methods in Engineering*, Vol. 31, No. 1, 1991, pp. 1–17, doi:10.1002/nme.1620310102.

[25] Nightingale, D., Ross, J., and Foster, G., "Cavity Unsteady pressure measurements - Examples from Wind-Tunnel Tests," Tech. Rep. Version 3, Aerodynamics & Aeromechanics Systems Group, QinetiQ, Bedford, UK, November 2005.

[26] Menter, F., Kuntz, M., and Bender, R., "A Scale-Adaptive Simulation Model for Turbulent Flow Predictions," *Proceedings of the 41st Aerospace Sciences Meeting and Exhibit*, Reno, Nevada, USA, 6-9 January 2003, doi:10.2514/6.2003-767.

[27] Heller, H., Holmes, D., and Covert, E., "Flow-Induced Pressure Oscillations In Shallow Cavities," *Journal of Sound and Vibration*, Vol. 18, No. 4, 1971, pp. 545 – 553, doi:10.1016/0022-460X(71)90105-2.

[28] Lee, B., "Effect of Captive Stores on Internal Weapons Bay Floor Pressure Distributions," *Journal of Aircraft*, Vol. 47, No. 2, March-April 2010, pp. 732–735, doi:10.2514/1.46684.

[29] Allen, R., Mendona, F., and Kirkham, D., "RANS and DES turbulence model predictions of noise on the M219 cavity at M=0.85," *International Journal of Aeroacoustics*, Vol. 4, No. 1, 2015, pp. 135–151, doi:10.1260/1475472053730039.

[30] Peng, S.-H., *M219 Cavity Flow*, *DESider A European Effort on Hybrid RANS-LES Modelling*, edited by W. Haase, M. Braza, and A. Revell, Vol. 103, Springer International Publishing, Berlin, Heidelberg, 2009, pp. 270–285, doi:10.1007/978-3-540-92773-0.

[31] Temmerman, L., Tartinville, B., and Hirsch, C., *URANS Investigation of the Transonic M219 Cavity*, *Progress in Hybrid RANS-LES Modelling: Papers Contributed to the 4th Symposium on Hybrid RANS-LES Methods, Beijing, China, September 2011*, edited by S. Fu, W. Haase, S.-H. Peng, and D. Schwamborn, Springer Berlin Heidelberg, Berlin, Heidelberg, 2012, pp. 471–481, doi:10.1007/978-3-642-31818-4_41.

[32] Smagorinsky, J., "General Circulation Experiments with the Primitive Equations," *Monthly Weather Review*, Vol. 91, No. 3, March 1963, pp. 99–164.

[33] Fox, J., "Generic Wing Pylon, and Moving Finned Store. TN. 37389-6001," Arnold Engineering Development Center (AEDC), Arnold AFB, USA, 2000.

[34] Dix, R. and Bauer, R., "Experimental and Theorical Study od Cavity Acoustics," Tech. Rep. AEDC-TR-99-4, Tenessee, United States, April 2000.

[35] Kim, D., Choi, J., and Kwon, O., "Detached eddy simulation of weapons bay flows and store separation," *Computers and Fluids*, Vol. 121, 2015, pp. 1–10, doi:10.1016/j.compfluid.2015.07.022.

[36] Cabral, B. and Leedom, L., "Imaging Vector Fields using Line Integral Convolution," *Proceedings of the 20th annual conference on Computer*

graphics and interactive techniques, SIGGRAPH, ACM, Anaheim, CA, United States, 1993, pp. 263–270.